Title: Myeloid mechano-metabolic programming restricts anti-tumor immunity

Authors: Tharp K.M.[1], Kersten K.[2,3], Maller O.M.[1], Timblin G.A.[1], Stashko C.[1], Hayward M-K. [1], Berestjuk I.[1], ten Hoeve-Scott J.[2], Samad B.[3-5], Combes A.J.[3-6], and Weaver V.M.[1,7]

[1]Center for Bioengineering and Tissue Regeneration, Department of Surgery, University of California San Francisco, San Francisco, CA 94143, USA

[2]UCLA Metabolomics Center, Department of Molecular and Medical Pharmacology, University of California, Los Angeles, Los Angeles, CA 90095, USA

[3]Department of Pathology, University of California San Francisco, San Francisco, CA 94143, USA

[4]ImmunoX Initiative, University of California San Francisco, San Francisco, CA 94143, USA

[5]UCSF CoLabs, University of California San Francisco, San Francisco, CA 94143, USA

[6]Department of Medicine, Gastroenterology division, University of California San Francisco, San Francisco, CA 94143, USA

[7]Department of Bioengineering and Therapeutic Sciences and Department of Radiation Oncology, Eli and Edythe Broad Center of Regeneration Medicine and Stem Cell Research, and The Helen Diller Family Comprehensive Cancer Center, University of California San Francisco, San Francisco, CA 94143, USA.

Abstract: Tumor progression ensues when the immune system fails to mount a productive anti-tumor response. Inappropriate programming of myeloid cells associates with tissue fibrosis and is accompanied by impaired T cell anti-tumor responses. Here, we demonstrate that myeloid cells respond to the stiffened fibrotic tumor microenvironment (TME) by initiating a wound-healing associated collagen biosynthesis program. A collateral effect of this programming is an untenable metabolic milieu for productive CD8 T cell anti-tumor responses, as collagen-synthesizing macrophages consume environmental arginine, synthesize proline, and excrete ornithine that compromises CD8 T cell function. Thus, a stiff and fibrotic TME may impede anti-tumor immunity not only by direct physical exclusion of CD8 T cells, but also via secondary effects of the myeloid mechano-metabolic programming described here that creates an inhospitable metabolic milieu for CD8 T cells.

Main Text: Cancer immunotherapy has revolutionized anti-cancer therapy. Nevertheless, these therapies are less effective against solid tumors because their efficacy depends upon the immune cell infiltration into the TME. Solid tumors are characterized by large quantities of physically dense extracellular matrix (ECM). The composition and physical properties of the dense ECM in solid tumors could mediate the physical exclusion of immunotherapy-requisite cytotoxic T lymphocytes (CTLs) populations [1,2] and stimulate recruitment of myeloid cell types [3] that impede anti-tumor programs of CTLs [4]. Therapies that block myeloid interference of CTL functions or infiltration into the TME hold great promise to enhance the efficacy of current immunotherapies [5] and make immunologically “cold” tumors “hot”. Immunologically “hot” tumors exhibit greater infiltration of CTLs that express PD-1 [6]. These types of CTLs predict greater rates of patient survival and are sensitive to therapeutic agents such as PD-1 checkpoint blockade, which potentiates PD-1^{+}CTL anti-tumor function and patient survival. PD-1 checkpoint blockade-based therapies have been found to be less effective in fibrotic tumors, which are characterized by an aberrant fibular-collagen rich ECM. Tumor-associated fibrosis is commonly

observed in breast cancer and correlates with reduced CTL infiltration and is driven by tumor infiltrating myeloid cells [7]. Therefore, understanding the relationships between myeloid cells, fibrosis, and CTL-suppressive programing in the tumor microenvironment is critical to enhance the efficacy of cancer immunotherapy in fibrotic tumors.

Tumor progression elicits collagen-ECM synthetic transcriptional programming in myeloid cells

Myeloid cells that infiltrate the TME and transition into tumor-associated macrophages (TAMs) can be a major impediment to effective anti-cancer immunotherapy because they release CTL-suppressive cytokines, engage in metabolism that competes CTL demands, and facilitate excessive ECM synthesis (fibrosis) that is correlated with reduced CTL tumor-infiltration [1,7,8]. Distinct subsets of TAMs exist which can be characterized by CD11c/CD11b expression levels and correspond with major histocompatibility complex II (MHCII) expression, as well as aspects of the *in vitro* polarization phenotypes (M1/M2) [9,10]. Recent scRNAseq efforts have demonstrated that TAMs possess greater diversity than these two historically defined subsets [11–13] . To study TAM population evolution during tumor progression, we used the spontaneous and immunocompetent MMTV-PyMT (Mouse Mammary Tumor Virus - Polyoma Virus Middle T Antigen) mammary tumor model. We isolated TAMs from early (8 week) and late stage PyMT spontaneous mammary tumors (11 week), and found that the CD11c/CD11b expression levels rather than proportional abundance to other immune cells in the TME changed during tumor progression (Fig. 1a-c). Although MHCII^{High}-TAMs are thought to oppose tumor progression and foster anti-tumor immune responses [14,15], we found that late stage TAMs shifted their expression profile to a pro-tumor M2-like (e.g., *Arg1*, *Vegfa*, and *Mrc1*) and collagen-ECM synthetic phenotype during tumor progression (Fig. 1c and s1a).

ECM composition, crosslinking, and topology play a major role in tumor progression and cellular programming in the TME [16–19] and we detected greater fibular collagen content in late stage tumors (Fig. s1b-c). Inhibiting lysyl oxidase (LOX)-mediated collagen crosslinks reduced the alignment and elastic modulus (stiffness) of fibular collagen, impeded tumor progression [18,19] and enhanced the efficacy of PD-1 based anti-tumor immunotherapies [20]. Because ECM stiffness has been correlated with altered expression profiles of TAMs [3,21] we inhibited LOX-mediated collagen crosslinking and used RNAseq to determine if the TAM transcriptional programming we observed was affected by the physical properties of the TME-ECM. We found that ECM stiffness was a key determinant of the expression levels of the collagen-ECM genes comprising the top gene ontology (GO) category affected by tumor progression (Fig. 1e). While cancer associated fibroblasts are the primary source of fibular collagen in the TME, TAMs do contribute specific collagens to the TME, such as the beaded filament collagen VI which forms microfibular networks that entrain epithelial basement membranes to interstitial ECM [22–24]. LOX-inhibition was sufficient to reduce the abundance of collagen VI in the interfacial layers of the tumor stromal border (Fig. s1d) which was a TAM transcript that was induced with progression, but reduced by LOX-inhibition. This finding is consistent with myeloid responses to the physical properties of foreign bodies (such as silicone breast implants), which alters transforming growth factor beta (TGFβ)-mediated fibrosis and collagen capsule formation [25,26].

To determine if human tumor infiltrating myeloid cells also express the murine tumor progression-induced collagen-ECM genes, and whether their expression affects anti-tumor immunity or patient outcomes, we correlated the expression profiles of myeloid cells isolated from 364 human tumors across 12 cancer types and with previously identified tumor-immune

states or “archetypes” spanning tissue of origin (Fig.1f) [27]. The analysis revealed that the expression of collagen transcripts in tumor infiltrating myeloid cells was lowest in Immune Rich and highest in Immune-Stromal and Immune Desert tumor-immune archetypes. These data suggest that expression of a collagen-ECM signature in myeloid cells is inversely correlated with productive anti-tumor immune responses and patient survival across many tumor types [27]. Using transcriptomes of 2506 human breast tumor samples (TCGA repository), we verified that the collagen-ECM signature was correlated with the M2-like polarization and not M1-like (Fig. 1g), similar to the association we observed in murine mammary tumor progression and the twelve human tumor types used to define the tumor immune archetypes. Expression of this collagen signature in Stage II and Stage IIIA untreated tumor biopsies correlated with reduced survival in breast cancer patients (p=0.0346) (Fig. 1h).

Mechanosignaling and TGFβ control collagen-synthetic transcriptional programming in TAMs

Previous studies from our lab showed that early stage resistin-like molecule α (*RELMα/RETNLA*) expressing TAMs, which is an early mark of activation in murine macrophage populations [28], secrete TGFβ1 that acts on stromal fibroblasts to establish fibrotic tumor ECM [7]. Autocrine TGFβ-signaling facilitates the transcriptional identity of tissue resident myeloid populations [29], which could explain the late-stage TAM transcriptional state (Fig. 1e). Because preventing ECM stiffening via LOX-inhibition attenuated the expression of many of these TGFβ-induced transcripts, and stromal stiffness can tune TGFβ-signaling in other cell types [30], we tested if the stiffness of fibular collagen affected TGFβ-signaling *in vitro*. Using M2-like polarized bone marrow derived macrophages (BMDMs receiving IL4 stimulation), we tested if TGFβ and fibular collagen stiffness affected *RETNLA* and Arginase (*ARG1*) expression, two genes which typically trend together in M2-polarization. TGFβ and fibular collagen stiffness synergistically and independently enhanced *ARG1* but synergistically suppressed *RETNLA* levels, consistent with our observation that the expression of these two genes was inversely abundant in the late stage TAMs within the highly stiff tumor stroma (Fig. s1e, similar to s1a). We found that the magnitude of TGFβ-induced SMAD signaling and the production of collagen VI produced by BMDMs was also dependent on the stiffness of fibular collagen (Fig. s1f-h). We also determined that BMDMs cultured on stiff fibular collagen generate more active TGFβ1 (Fig. s1i), which could explain the late stage TAM phenotype.

We next used an unbiased approach to define what controls the expression of the tumor progression-associated collagen transcripts in TAMs. Promoter motif analysis of the genes comprising the top GO category predicted that they were primarily regulated by SMADs and SP1, a transcriptional response known to occur downstream of TGFβ-signaling (Fig. s2a). Because TGFβ signaling in the stiff collagen TME could explain the *ARG1/RETNLA* and collagen-ECM transcriptional state in TAMs, we generated a genetically engineered mouse model to test if abrogating TGFβ-signaling in myeloid cells (LysM-cre x TGFβRII$^{flox/flox}$, TGFβRII^{MyeKO}) could diminish the collagen-ECM phenotype. By transplanting PyMT mammary tumor cells into this mouse model and its corresponding control animals (Fig. 2a), we found that TGFβ-signaling in TAMs was responsible for, at least, the abundance of collagen VI and XII in the TME. We observed many TAMs and collagen VI localized to the interfacial layers of ECM between the tumors and surround stroma, while collagen XII was evenly distributed throughout the TME (Fig. 2c s2b). Orthotopic PyMT tumors generated with soft of stiff fibular collagen

demonstrated that TGFβRII^{MyeKO} reduced primary tumor growth in stiff fibular collagen TMEs (Fig. s2c) and reduced the prevalence and size of metastatic lesions in the lungs (Fig. s2d).

Because a previous report showed that the TGFβRII^{MyeKO} model is refractory to lung colonization in a CD8 CTL-dependent fashion [31], we checked if there were more CD8 CTLs infiltrating the TGFβRII^{MyeKO} primary tumors. Indeed, we found a greater quantity and proportion of the tumor infiltrating lymphocytes were CD8 CTLs (Fig. 2d-e). When we assessed the spatial distribution of these CD8 CTLs, we found that the TGFβRII^{MyeKO} orthotopic tumors had CD8 CTLs distributed throughout the stiff collagen tumors, but very few beyond the tumor-stroma border zone in the control animals (Fig. 2f). Similarly, we found less apoptotic (cleaved caspase-3^{+}) cells in stiff collagen control tumors and more in stiff collagen TGFβRII^{MyeKO} tumors or soft collagen control tumors, which suggests a more productive anti-tumor immune response. Due to the widely observed inverse correlation of fibular collagen content to the abundance of CD8 CTLs in tumors, it has been hypothesized that tumors with stiff and elaborate fibular collagen networks are refractory to CD8 CTL infiltration because the collagen physically blocks CD8 CTL infiltration. However, because we were able to detect CD8 CTLs infiltrating beyond the tumor-stroma border in the stiff fibular collagen TGFβRII^{MyeKO} orthotopic tumors, we decided to explore an alternative explanation to fibular collagen-mediated physical exclusion.

Mechanosignaling and TGFβ control collagen-synthetic metabolic programming in macrophages

It has become clear that activated T lymphocytes have unique metabolic demands to support their effector functions and survive in the TME [32]. Specific metabolic programs are essential for immune cells to achieve discrete phenotypes or functions [33–35], and the available metabolites can dictate whether a cell can utilize a particular metabolic pathway to achieve an optimal phenotype or function [32,36–38]. Since ECM stiffness exerts significant effects on cellular metabolism [16], we profiled polar metabolites in stiff fibular collagen and LOX-inhibited tumors to identify potential changes in the TME metabolic milieu associated with decreased fibular collagen-ECM stiffness that might influence the phenotype or function of infiltrating immune cells. Auspiciously, we found that preventing collagen crosslinking and stromal stiffening via LOX-inhibition caused a ~4-fold increase in the concentration of arginine in the TME (Fig. 3a). Previous studies of tumor interstitial fluid have implicated a depletion of arginine in tumors relative to normal tissues, as well as a seemingly direct relationship between arginine depletion and ornithine enrichment in the TME [39].

Myeloid cells expressing high levels of *ARG1* have been implicated as major consumers of arginine in the TME [40,41], but it is unclear what the purpose of this arginine metabolism is. Incidentally, collagen synthesis requires unique metabolic support because collagen contains a disproportionally high abundance of proline (~8 fold higher than proteome median), which can be synthesized from arginine or glutamine. Exogenous proline supplementation does little to increase collagen synthesis in healing wounds, but its levels increase in healing wounds relative to plasma concentrations [42]. However, supplementation with arginine enhances collagen deposition and tensile properties of healing wounds [43] and has shown clinical efficacy in treating “hard-to-heal” wounds in elderly and diabetic patients [44], but this effect has not been directly shown to occur via arginine metabolism to proline. Mindful of this relationship, we re-examined the tumor metabolomics and found that corresponding to the increased levels of arginine (Fig. 3a) there were commensurate decreases in proline and ornithine, products of arginine metabolism, upon LOX-inhibition (Fig. 3b).

In addition to regulating collagen gene expression, TGFβ-signaling enhances proline synthesis [45] via glutamine and arginine metabolism [46]. To determine if myeloid TGFβ-signaling affected the proportions of arginine:ornithine:proline in tumors, we assayed polar metabolites in the TME of TGFβRII^{MyeKO} tumors and their corresponding controls. We found that while levels of arginine were unaffected, ornithine and proline levels were significantly reduced in TGFβRII^{MyeKO} tumors (Fig. 3c) implicating TAM-TGFβ signaling as a significant regulator of the intratumoral levels of these metabolites. The fact that arginine levels were not different in TGFβRII^{MyeKO} tumors, but were in the LOX-inhibited tumors suggests that other cell types in TME metabolize arginine in a mechanosensitive fashion. To verify that TGFβ-signaling influenced myeloid utilization of exogenous arginine, we assayed M2-like BMDMs treated with or without TGFβ and found that TGFβ enhanced arginine uptake, but also ornithine efflux into the culture medium (Fig. 3d). We then directly tested if ECM stiffness and TGFβ enhanced arginine conversion into proline by supplementing IL-4-polarized BMDMs with $^{13}C_6$-arginine and measuring proline (m+5) (which indicates the direct flow of carbon derived from arginine into de novo proline synthesis) (Fig. 3e). Proline synthesis rates from arginine metabolism and steady-state proline-OH levels were both synergistically enhanced by TGFβ and ECM stiffness, whereas intracellular ornithine levels were only elevated by ECM stiffness, and steady-state proline levels were specifically elevated in response to TGFβ (Fig. 3f and s3a-b). Because de novo proline synthesis can also be fed by glutamine metabolism, which is mechano-sensitive [47], we assayed if ECM stiffness influenced glutamine conversion into proline. Strikingly, we found that stiff fibular collagen caused a ~5-fold higher incorporation of ^{13}C into proline from $^{13}C_5$-glutamine (Fig. 3h) indicating that the two primary pathways implicated in de novo proline synthesis were both mechanosensitive and TGFβ-dependent.

It has been proposed that proline synthesis serves as vent for excess mitochondrial reducing equivalents (e.g., NADH and NADPH) when mitochondrial respiration is suppressed. Mitochondrial oxidative flux and the activity of pyrroline-5-carboxylate reductase 1 (PYCR1), required to synthesize proline in the mitochondria, have been shown to be mechanosensitive in other cell types [16,48]. We found that TGFβ suppressed mitochondrial respiration (Fig. s3c) and NADH levels were synergistically enhanced by TGFβ and ECM stiffness (Fig. s3d). Although we did not observe an ECM stiffness dependent enrichment of PYCR1 in the mitochondria in these myeloid cells, we did observe an overall increase in mitochondrial content in the cells interacting with the stiff fibular collagen ECM. These findings imply that the increased proline synthesis we detected in IL-4-polarized BMDMs cultured on a stiff ECM was primarily driven by elevated levels of NADH, similar to what has been found in fibroblasts [45].

Ornithine impairs CD8 CTL metabolism and anti-tumor activity

Commensurate with arginine consumption in TAMs and IL-4-polarized BMDMs, was an increase in environmental ornithine in the TME or culture medium. Arginine is an essential metabolite for activated lymphocyte survival and anti-tumor responses [32]. In fact, conditioning tumors with arginine synthetic bacteria, that consume ornithine and ammonia to synthesize arginine, potentiates cancer immunotherapies reliant on activated CTLs [49]. Models of T cell activation using CD3/CD28 antibodies have demonstrated that activation triggers distinct metabolic programing. To explore how ornithine affected CD3/CD28-activated CD8 CTL metabolism, we titrated the concentration of ornithine relative to arginine (~1:1, 3:1, and 9:1 that mimics the effect observed in Fig.3 tumors) and measured intracellular polar metabolites with mass-spectrometry based metabolomics. We found that after 24 hours of activation, increased

concentrations of ornithine resulted in a decrease in ATP and elevated levels of intracellular ornithine, its downstream metabolites (e.g., citrulline), and arginine (Fig. s4a). While it is not clear why arginine is the favored metabolic substrate in activated CTLs, if arginine metabolism is suppressed and ATP levels fall, translation (high ATP demand) could be impeded and the synthesis of effector proteins stalled retarding anti-tumor programming. Peak utilization of arginine has been shown to occur ~ 72h after activation. Accordingly, we assayed the metabolome of CD8 CTLs after 3 days of culture in an environment containing a molar ratio of ~3:1 ornithine:arginine. Nearly all metabolite pools were suppressed by environmental ornithine, except for oxidized glutathione (GSSG) (Fig. 4b) which negatively affects survival and inflammatory programming of CTLs [50,51].

To determine if environmental ornithine levels affected antigen-specific CD8 CTL anti-tumor responses, we utilized PyMT-mCherryOVA tumor cells [52] that express the model antigen chicken ovalbumin (OVA) and transgenic OT-I CD8 T cells that specifically recognize the OVA-derived SIINFEKL peptide. OVA-PyMT tumor organoids formed in stiff collagen or cultured as a monolayer on glass coverslips were challenged with GFP-OT-I cells in the presence of varied concentrations of ornithine (Fig 4b and s4b). Tumor cells cultured in the presence of ornithine appear resistant to OT-I-mediated death (e.g., cleaved caspase-3$^+$) and the only GFP-OT-I cells we could find were either ~ 1-3 um fragments with no observable nuclei (debris-like) or in the process of becoming cleaved caspase-3$^+$ themselves. Because *in vitro* models do not consistently recapitulate living tissues, we next tested if dietary supplementation could be used to raise the concentration of ornithine or arginine in circulation of the orthotopic MMTV-PyMT mammary tumor model (Fig s4c). Supplementation with ornithine raised the concentration of plasma ornithine ~12-fold, NAD$^+$ 4-fold, but it did not affect citrulline. Supplementation with arginine elevated circulating arginine and ornithine ~3.5-fold and did not significantly affect citrulline levels. As a control, we tested both water and glycine, which did not affect circulating levels of ornithine or arginine, but glycine supplementation did modestly raise citrulline levels.

Dietary supplementation with ornithine, arginine, or glycine did not affect orthotopic PyMT tumor size, but more circulating tumor cells were detectable in ornithine supplemented animals (Fig. s4d). Ornithine supplementation dramatically reduced the expression of activation markers, PD1 and CD69, on endogenous CD44$^+$ tumor infiltrating CD8 CTLs (activated), whereas arginine supplementation maintained PD1 and CD69 levels in spite of also elevating circulating ornithine levels (Fig 4d-e and s4f). Moreover, ex vivo stimulated CD8 CTLs from these tumors were found to be less proliferative (Fig. 4f), suggesting that ornithine impairs anti-tumor T cell responses. Because PD1 expression typifies an immunologically “hot” tumor that may be responsive to checkpoint blockade-based immunotherapies and ornithine supplementation suppressed PD1 expression in PyMT tumors, we sought to test if PD1 blockade was sensitive to the circulating levels of ornithine. While ornithine, arginine, or glycine supplementation alone did not affect orthotopic PyMT tumor growth, they did affect tumor growth rates of mice treated with anti-PD1 checkpoint blockade. Ornithine supplementation abolished the beneficial effects of anti-PD1 blockade and tumors grew to their humane terminal endpoint as fast as isotype-control animals (Fig. 4h), whereas checkpoint blockade in the context of arginine and glycine supplementation had a ~33% increase in median survival time (Fig. 4i).

Discussion

Cancer-associated fibrosis is thought to support tumor progression by serving as a physical barrier to the anti-tumor adaptive immune system. However, T cells can migrate through sub-micron spaces when extravagating into inflamed tissues or through engineered pore sizes much smaller than highly cross-linked fibular collagen matrices, implying that cross-linked fibular collagen unlikely impedes T cell infiltration [53–56]. Because TAMs enrich in stiff and fibular collagen-rich regions of tumors, where they synthesize network-forming collagens supported by arginine metabolism, our findings indicate that mechano-metabolic programming of TAMs likely plays an unappreciated role in the suppression of CTL anti-tumor responses by establishing an inhospitable metabolic milieu associated with fibrosis and ECM synthesis. Early infiltrating TAMs promote the development of tumor-associated fibrosis by conditioning the TME with TGFβ1, which acts on stromal fibroblasts to synthesize fibular collagens and collagen crosslinking enzymes leading to a stiffened TME [7]. The physical properties of the ECM affect TAM recruitment [3,57], promote tumor aggression [58], and metabolic reprogramming of tumor cells [16] and infiltrating immune cells. Our data indicate that as tumors progress, the stiffened TME and TGFβ-signaling tune the transcriptional and metabolic programming of TAMs to efficiently synthesize network-forming ECM components that entrain fibular collagens and facilitate wound healing, scar tissue formation, re-epithelialization, and metastatic progression [59,60]. Taken together, these observations indicate that TAMs contribute to cancer-associated fibrosis in collaboration with stromal fibroblasts through iterative phases of fibular and network forming ECM-synthesis.

Numerous studies have demonstrated that TAMs impair CTL anti-tumor responses and diminish the efficacy of checkpoint blockade [61,62]. However, not all TAMs exert repression on the adaptive immune system or promote tumor growth. TAMs programmed or reprogrammed through T helper type 1 (Th1)-associated cytokines can become tumoricidal themselves and this is transiently associated with a de-repressive effect on adaptive immune system [63]. Similarly, T helper type 2 (Th2)-associated cytokines (e.g., TGF-β1) facilitate pro-tumor TAM phenotypes and limit the efficacy cancer immunotherapies in fibrotic tumors [1,2,64]. M1/Th1 and M2/Th2 metabolism differentiates the fate of arginine (e.g., ornithine), and arginine supplementation enhances anti-tumor CTL responses, particularly in the context of checkpoint blockade [49]. Our findings illustrate that in collaboration with M2/Th2 cytokines, mechano-metabolic programming induced by the fibular collagen content of the TME influences the metabolism of arginine and the abundance of ornithine. Our data indicate that the combination of fibrosis and M2/Th2 cytokines dictate the ratio of arginine:ornithine in the TME, establishing syn/anti-trophic (cross-feeding/starving) metabolism from TAMs to lessen the cytotoxic activity adaptive immune cells, support stromal ECM synthesis, or promote the growth and survival of cells experiencing metabolic stress [65].

The unresolved question from our work is why would the physical properties of the TME promote collagen-ECM synthetic TAM phenotype at the expense of anti-tumor inflammation? We hypothesize that the physical properties of the TME subvert anti-tumor (inflammation, M1/Th1) in favor of pro-tumor (ECM synthetic, M2/Th2) TAM programming due to an evolutionarily-beneficial, but maladaptive-in-the-tumor-context, wound-healing response trigged by the fibular ECM content of the TME or site of injury. Open and closed wounds initially display inflammatory programs regardless of sterility. These inflammatory programs are initiated by endogenous Damage Associated Molecular Patterns (DAMPs) in sterile wounds that collaborate with exogenous pattern associated molecular patterns (PAMPs) in open wounds to elicit inflammatory programs that remodel the site of injury for efficient surveillance and clearance of the sources of PAMPs/DAMPs. However, inflammatory programming is not static, as

PAMPs/DAMPs are cleared, temporary reconstructive scaffolding (e.g., fibrin) is used to physically support the site of inflammation that is subsequently replaced by a more permanent fibular collagen matrix. This fibular collagen matrix is synthesized and mechanically entrained by neighboring cells (e.g., fibroblasts or keratinocytes), and it can dictate the recruitment of immune cells [57] or a programmatic homeostasis between stromal cell types [66]. Similar to wound healing responses, the inflammatory programming of myeloid cells is not static. Dynamic phenotypic transitions occur in phases at sites of injury where myeloid-derived cells that initially expressed DAMP-driven M1/Th1-like characteristics transition into M2/Th2-like states to produce TGFβ1 [67] and synthesize specific types of ECM that facilitate and typify the resolution of wound healing [68].

Physically, the similarities between the phased responses observed in wound healing or tumor progression are intuitively obvious. The early inflamed (i.e., PAMP/DAMP enriched) microenvironment is soft due to loss of tissue structure and cell death or clearance. As inflammatory signals are cleared or tolerated [69], ECM synthesis and cell contractility mediate tissue stiffening in specific regions of the TME (e.g., invasive borders). Microenvironmental physical cues synergize with PAMP/DAMP-signaling to inform infiltrating cells to express transcriptional phenotypes intended to match the stage of healing (e.g., fibronectin is a TLR4 ligand, that becomes inaccessible once incorporated into fibular matrix). Physical properties of healing wounds reflect the stage of repair, where a stiff wound has reached the phase in which the source of DAMP/PAMP has been cleared, and the wound is structurally entrained to its surrounding tissue. Our data suggest that one way that the physical properties of the TME drives TAMs to a pro-tumor/repair phenotype is by dictating the metabolic fate of arginine, which is a hallmark difference between M1/Th1 and M2/Th2 phenotypes of myeloid cells [70]. Myeloid arginine metabolism serves an immunomodulatory role by restricting the proliferation and activity of T-cells [71], which may serve to lessen inflammatory responses in healing wounds or progressing tumors [72]. M2/Th2 associated arginase (*ARG1*) catalyzes the conversion of cytosolic arginine into ornithine, which can then enter the mitochondria via SLC25A15/SLC25A2-mediated transport [73] to serve as a substrate for proline synthesis. Arginine-ornithine exchange in lower organisms occurs in a 1-to-1 ratio [74], and the mammalian exchanger SLC15A15 has been shown to mark a subset of myeloid-derived TAMs that are 8-fold more prevalent in tumors than healthy tissues [75]. Overall, our results suggest that mechano-metabolic programming induced by the physical properties of a tissue may instruct and support infiltrating myeloid cell programming to match a presumed stage of wound healing, which is speciously subverted in tumor progression.

Arginine supplementation is sufficient to potentiate anti-tumor immunity and efficacy of checkpoint blockade therapies [49]. However, ingested arginine can be metabolized in the gut or liver, generating ornithine, which can exert suppressive effects on CTL proliferation and activation [76]. We found that arginine supplementation increased the circulating concentrations of ornithine while also exerting beneficial effects on CTL function, which may have had greater benefit if the ornithine levels did not also increase. Systemic ornithine supplementation had an immunomodulatory effect on TILs similar to manipulations which affected the ratio of ornithine:arginine in the TME. Chronic viral infections of the liver have been shown to increase circulating ornithine levels which impede virus-specific T cell expansion, indicating that ornithine is an immunomodulatory metabolite for CTLs locally and systemically [77]. Taken together, therapies that could increase arginine through consumption of ornithine may have the greatest impact to enhance checkpoint blockade therapies and anti-tumor immunity. One such therapy has been shown to improve checkpoint blockade via local synthesis of arginine by a synthetically-engineered strain of Escherichia coli Nissle 1917 (ECN) that was designed to consume environmental ammonia and excrete arginine in the TME [49]. While this approach has

not yet been shown to consume ornithine, ECN readily metabolizes ornithine and this engineered strain has been optimized to convert ornithine to arginine, and not polyamines or other catabolic endpoints. Such findings indicate that this arginine synthetic ECN stain may inadvertently tune the balance of arginine:ornithine in the TME, and this may be foundational to productive CTL response in solid tumors. Alternatively, inhibiting the metabolic programs in TAMs which facilitate arginine conversion to ornithine may have beneficial effects on anti-tumor immunity. Nevertheless, caution should be used as this might occur at the expense of effective wound healing responses, and thus may be inappropriate to use in combination with surgery.

Acknowledgments:

Funding: This work was supported by 1F32CA236156-01A1, 5T32CA108462-15, and Sandler Program for Breakthrough Biomedical Research (postdoctoral Independence award) to K.M.T.; R35 CA242447-01A1, R01CA192914, and R01CA222508-01 to V.M.W.

Author contributions: Conceptualization: K.M.T. & V.M.W. Methodology: K.M.T, Investigation: K.M.T., K.K., O.M., G.T., C.S., J.t.H-S. Formal Analysis: K.M.T., K.K., C.S., B.S., A.C., & J.t.H-S. Data curation: K.M.T. Funding acquisition: V.M.W., K.M.T, Project administration: K.M.T. Resources: Software: C.S. Supervision: V.M.W. Validation: K.M.T., K.K., G.T, and C.S. Visualization: K.M.T. Writing – original draft: K.M.T. Writing – review & editing: K.M.T., V.M.W., K.K. G.T., & A.C.

Declaration of Interests: The authors declare no competing interests.

Methods

Cell culture

Bone marrow was isolated from 8-12 week old C57BL6/J femurs (via dissection and syringe-mediated PBS hydraulic pressure) and cultured in 25 mM glucose DMEM (Gen Clone, 25-500) supplemented with 10% Fetal Bovine Serum (FBS) (Hyclone, SH30071.03) and penicillin/streptomycin (Gibco, 151140-122) with 25 ng/mL recombinant murine Macrophage Colony Stimulating Factor (mCSF-1) (Peprotech, 315-02) for 7 days (media changes every 3 days, first 20 mL then 25 mL) in 15 cm^2 tissue culture polystyrene culture plates (Gen Clone, 25-203) to generate bone marrow derived macrophages (BMDMs).

$CD8^+$ CTLs were isolated from the spleen, inguinal and axillary lymph nodes of 8-12 week old C57BL6/J or OT1 mice (C57BL/6-Tg(TcraTcrb)1100Mjb/J, JAX:003831). Tissues were pulverized with a 1 mL syringe plunger through a PBS wetted 70 µm cell strainer (Corning, 352350). The resulting cell suspension was treated with ACK lysis buffer [150 mM NH_4Cl, 10 mM $KHCO_3$, 0.1 mM Na_2EDTA, pH 7.3] to remove red blood cells and $CD8^+$ T cells were isolated via EasySep Mouse CD8+ T Cell Isolation Kit (Stemcell Technologies,19853) per manufacturer's instructions. $CD8^+$ T cells were activated with Dynabeads Mouse T-Activator CD3/CD28 for T-Cell Expansion and Activation (Gibco, 11456D) without exogenous recombinant IL2 supplementation. OTI $CD8^+$ T cells were isolated and co-cultured with PyMT-mCherryOVA tumor cells [52] that display the model antigen chicken ovalbumin (SIINFEKL) in 25 mM glucose DMEM (Gen Clone, 25-500) supplemented with or without L-ornithine (RPI, 020040).

ECM coated polyacrylamide hydrogel cell culture surfaces (PA-gels)

Cleaned (10% ClO, 1M HCL, then 100% EtOH) round #1 German glass coverslips (Electron Microscopy Services) were coated with 0.5% v/v (3-Aminopropyl)triethoxysilane (APTES, Sigma, 440140), 99.2% v/v ethanol, and 0.3% v/v glacial acetic acid for 2 h and then cleaned in 100% EtOH on an orbital shaker at 22 ºC. APTES activated coverslips were coated with PBS

buffered acrylamide / bis-acrylamide (Bio-Rad, 1610140 and 1610142) solutions (3% / 0.05% for 400 Pa, 7.5% / 0.07% and 10% / 0.5% for 60k Pa) polymerized with TEMED (0.1% v/v) (Bio-Rad, 1610801) and Potassium Persulfate (0.1% w/v) (Fisher, BP180) to yield a final thickness of ~ 85 µm. PA-gels were washed with 70% EtOH and sterile PBS prior 3,4-dihydroxy-L-phenylalanine (DOPA) coating for 5 min at 22 ºC protected from light with sterile filtered DOPA in pH 10 [10 mM] Tris buffer [78]. DOPA coated PA-gels were washed 2x with sterile PBS and ECM functionalized with 10 µg/mL Type I collagen (Corning, 354236) in sterile PBS 1 h at 37 ºC.

Fibroblast derived ECM culture surfaces

Fibroblast derived ECM (fECM) was generated based on previously described methods [79]. Multipotent subcutaneous adipose derived fibroblasts [80] were seeded in gelatin-coated tissue culture dishes, cultured for 8 days in a complete medium (DMEM 10% FBS, 1% A/A) with 1 ng/mL TGFβ1 and 50 µg/ml ascorbic acid added every 48 h to support collagen synthesis. Cell cultures were washed with PBS and de-cellularized using a pre-warmed (37˚C) extraction buffer for 2-5 min (0.5% Triton X-100, 20 mM NH4OH in PBS). Residual ECM were then washed three times with PBS prior to seeding BMDMs on top of the fECM.

qPCR

Total RNA was isolated from biological samples with TRIzol (Invitrogen, 15596-018) according to the manufacturer's instructions. cDNA was synthesized with 250 ng total RNA in 10 µL reaction volume with RNA using M-MLV reverse transcriptase (BioChain, Z5040002-100K) and 5X reaction buffer (BioChain, Z5040002-100K), random hexamers (Roche, 11034731001), dNTPs , and 1U of Ribolock (ThermoFisher, EO0384). RT-thermocycler program: random hexamers and RNA incubated at 70ºC for 10 min, then held at 4ºC until the addition of the M-MLV reverse transcriptase, dNTPs, Ribolock, and M-MLV-reverse transcriptase, then 50 ºC for 1 h, 95 ºC for 5 min, then stored at -20 ºC until qPCR was performed. The reverse transcription reaction was then diluted to 50 µL total volume with ddH_2O rendering a concentration of 20 ng RNA per 1 µL used in subsequent qPCR reactions. qPCR was performed in triplicate using PerfeCTa SYBR Green FastMix (Quantabio, Cat# 95072-05K) with an Eppendorf Mastercycler RealPlex^2. qPCR thermocycler program: 95° C for 10 min, then 40 cycles of a 95°C for 15 s, 60°C for 20 s, followed by a melt curve 60-95°C over 10 min. Melt curves and gel electrophoresis were used to validate the quality of amplified products. The ΔCt values from independent experiments were used to calculate fold change of expression using the $2^{-\Delta\Delta Ct}$ method. For each gene measured, the SEM of the ΔCt values was calculated and used to generate positive and negative error values in the $2^{-\Delta\Delta Ct}$ fold change space. Plots of qPCR data display bars representing the mean fold change ±SEM and individual points representing the fold change value for each experiment relative to the mean.

qPCR primers used:

	5'-Forward	**5'-Reverse**
PyMT	GCCTATAGACTGGCTGGACC	CTCTCCTCAGTTCCTCGCTCC
ARG1	ATCGGAGCGCCTTTCTCAAA	AAGTTTTTCCAGCAGACCAGC
RETNLA	GGTCAAGGAACTTCTTGCCAAT	GGAGGCCCATCTGTTCATAGTC
HPRT	TCAGTCAACGGGGGACATAAA	GGGGCTGTACTGCTTAACCAG
18S	GAGAAACGGCTACCACATCC	CCCAAGATCCAACTACGAGC

In vitro respirometry

Mitochondrial stress tests were performed with a Seahorse XF24e cellular respirometer on non-permeablized cells (50k cells/well) in V7 microplates, with XF assay medium supplemented with 1 mM pyruvate (Gibco), 2 mM glutamine (Gibco),and 5 or 25 mM glucose (Sigma) at pH 7.4 and

sequential additions via injection ports of Oligomycin [1 µM final], FCCP [1 µM final], and Antimycin A/Rotenone [1 µM final] during respirometry (concentrated stock solutions solubilized in 100% ethanol [2.5 mM] for mitochondrial stress test compounds). OCR values presented with non-mitochondrial oxygen consumption deducted.

RNAseq

RNA-seq data from TAMs were generated with PyMT mammary tumors collected in DMEM on ice then minced with a prison shank-like razor blade. Tissues were digested in two 30 min rounds of collagenase and DNase with agitation at 37ºC. At the end of each round, digested tissue was washed through a 100 µm cell strainer on ice. Red blood cells were lysed with ACK buffer [150 mM NH_4Cl, 10 mM $KHCO_3$, 0.1 mM Na_2EDTA, pH 7.3] and remaining cells washed and counted. Cells were stained with anti-mouse CD45, anti-mouse CD11b, anti-mouse Ly6C, anti-mouse CD14, anti-mouse I-A/I-E, anti-mouse CD11c, anti-mouse CD24, anti-mouse CD29, anti-mouse CD31, and Zombie NIR live/dead. Sorted macrophages were $CD45^+$, $MHCII^+$, $CD14^+$. Sorted cells were pelleted and snap frozen on dry ice. RNA was harvested using Trizol and measured on a spectrophotometer and run out on a Bioanalyzer to confirm quality. Libraries were prepared according to manufacturer instructions using Nugen Ovation plus Nextera. Multiplexed libraries were sequenced on an Illumina HiSeq4000, and reads were aligned to the human genome (hg19) using RNA STAR [81]. Aligned reads were counted using HOMER [82] , and hierarchical clustering was performed using Cluster [83] and visualized with Java TreeView. Gene Ontology and motif analysis was performed using Metascape [84]. GEO Accession: GSE157290.

RNA-seq data from human tumors was re-analyzed for myeloid expression levels of transcripts associated with the collagen-containing ECM GO category, data published previously [27] (GEO Accession: GSE184398). Additionally, transcriptomic data for the BRCA, GBM, KIRC, LUAD, and PAAD projects were acquired from the TCGA repository. To control for the disparity in total RNA collected for each sample, observed library sizes were scaled into effective library sizes via the TMM method [85] in calcNormFactors (edgeR v3.34.1). Briefly, TMM assumes that most genes are not differentially expressed between samples and scales gene-level counts to alleviate artifactual expression differences that arise due to differing initial RNA abundances and sequencing depths. RNAseq counts were filtered to remove lowly expressed genes, then normalized using calcNormFactors (edgeR v3.34.1) and GSVA (v1.40.1) was applied to estimate enrichment of collagen genes as well as macrophage M1- and M2-like signatures [27].

Picrosirius red staining and polarized light microscopy

Formalin Fixed Paraffin Embedded (FFPE) tissue sections were stained using 0.1% picrosirius red (Direct Red 80, Sigma, 365548) in picric acid solution (Sigma, P6744) and counterstained with Weigert's hematoxylin (Cancer Diagnostics, catalogue number CM3951). Polarized light images were acquired using an Olympus IX81 microscope fitted with an analyzer (U-ANT) and a polarizer (U-POT, Olympus) oriented parallel and orthogonal to each other.

LC-MS metabolomics and arginine- or glutamine-derived ^{13}C-flux

500k BMDMs were seeded on 50 mm^2 varied stiffness ECM coated PA-gels and cultured for 24h in 25 mM glucose DMEM or 20-22 h in 25 mM glucose DMEM followed by medium change to DMEM lacking glutamine (Gibco, 11960044 replaced with with $^{13}C_5$-glutamine (Cambridge Isotope Laboratories, CLM-1822-H-PK) for 2 h, or in SILAC DMEM medium (Gibco, 88364), lacking arginine and lysine, replaced with $^{13}C_6$-arginine (Cambridge Isotope Laboratories, CLM-2265-H-PK) and L-lysine (sigma, L5501) for 4 h. 500k activated $CD8^+$ T cells (CD3/CD28 Dynabeads) were cultured in DMEM supplemented with L-ornithine for prescribed time points with medium changed after 48 h for the 3 day activation. Cells were washed twice with PBS and extracted with mass spectrometry grade 80% methanol (Fisher, A456-1) and 20% water (Fisher,

W6500) supplemented with 1 nmol DL-Norvaline (Sigma, N7502). Flash frozen tumors/tissues were pulverized with liquid nitrogen in a mortar and pestle on dry ice, 400 µg protein equivalents of tissue were extracted with mass spectrometry grade 80% methanol (Fisher, A456-1) and 20% water (Fisher, W6500) supplemented with 1 nmol DL-Norvaline (Sigma, N7502). Tissue or Insoluble material from cell extracts were used to calculate protein equivalents by resuspension in 0.2 M NaOH, heated to 95 ºC for 25 min, and determined via BCA (Pierce, 23225). Dried metabolites were resuspended in 50% ACN:water and 1/10th of the volume was loaded onto a Luna 3 um NH2 100A (150 × 2.0 mm) column (Phenomenex). The chromatographic separation was performed on a Vanquish Flex (Thermo Scientific) with mobile phases A (5 mM NH_4AcO pH 9.9) and B (ACN) and a flow rate of 200 µL/min. A linear gradient from 15% A to 95% A over 18 min was followed by 9 min isocratic flow at 95% A and reequilibration to 15% A. Metabolites were detected with a Thermo Scientific Q Exactive mass spectrometer run with polarity switching (+3.5 kV / -3.5 kV) in full scan mode with an m/z range of 65-975. TraceFinder 4.1 (Thermo Scientific) was used to quantify the targeted metabolites by area under the curve using expected retention time and accurate mass measurements (< 5 ppm). Values were normalized to cell number and sample protein concentration. Relative amounts of metabolites were calculated by summing up the values for all isotopologues of a given metabolite. Fractional contributional (FC) of ^{13}C carbons to total carbon for each metabolite was calculated as previously described [86]. Data analysis was accomplished with an in-house developed R scripts.

Immunofluorescence microscopy

Cells or tissues were fixed in 4% paraformaldehyde (Electron Microscopy Services, 15710) in PBS for 30 min at room temperature for cell cultures or overnight at 4 ºC for tissues, washed and blocked with a blocking buffer (HBSS fortified with: 10% FBS (Hyclone), 0.1% BSA (Fisher, BP1600), 0.05% saponin (EMD, L3771), and 0.1% Tween 20 (Fisher, BP337500). Primary antibodies [1:100-1:200] for 2 h at RT (22-23 ºC) or 24 h at 4 ºC, Secondary antibodies [1:1000] for 2 h at RT. Samples were imaged with a Nikon Eclipse Ti spinning disc microscope, Yokogawa CSU-X, Andor Zyla sCMOS, Andor Multi-Port Laser unit, and Molecular Devices MetaMorph imaging suite. Antibodies: Cleaved Caspase 3 (Cell Signaling, 9661), Collagen XII (Sigma, SAB4500395), Collagen VI (Abcam, ab6588), PyMT9 SCBT, PyMT (SCBT, sc-53481), and F4/80 (Cell Signaling, 70076).

Fibular collagen tumor organoids and orthotopic tumors

Collagen type I [4.8 mg/mL final] (Rat-tail, Corning, 354249) was suspended in 0.1% glacial acetic acid with (stiff) or without (soft) non-metabolizable L-ribose [0.5 mM final] (Chem Impex International, 28127) for at least 28 days at 4 ºC to facilitate complete collagen glycation/crosslinking [18]. To generate orthotopic tumors or 3D-tumor cell organoids, 1 M/mL PyMT tumor cells were suspended in collagen +/- L-ribose supplemented with basement membrane extract [20 % v/v final (R&D Systems, Cultrex BME, 3532-005-02) and DMEM [1x final] and the pH was adjusted to ~7.3. Tumor cell-collagen suspensions were kept on ice until implantation via 25 g syringe (100 µL per animal) or pipetted (20 µL) into culture dishes containing growth media for in vitro tumor organoid cultures.

Primary tumor growth, circulating tumor cells, and lung metastasis

Tumor growth was monitored by caliper measurement and volume estimation based on V = (W2 × L)/2 or absolute measurement of mass. Lung metastases were quantified by counting of surface lesions at time of animal sacrifice, and by examination of histological lung sections stained by H&E. Lungs were scanned using a ZEISS Axio Scan.Z1 digital slide scanner

equipped with CMOS and color cameras, 10x, 20x and 40x objectives, and lesion area was determined by tracing metastatic lesions in QuPath114.

Amino acid supplementation and PD-1 checkpoint blockade

Fibular collagen orthotopic tumors were generated with 100k PyMT cells in 100 µL collagen suspension per mouse, implanted via 25g syring injection into the 4/5 mammary fat pad of 8 week old female C57BL6/J mice. Every day until humane endpoint the mice were gavaged with 100 µL water or 2 g/kg glycine (Fisher, BP3815), ornithine (RPI, 020040), or arginine (TCI, A0528) suspended in water (~100 µL). For PD-1 checkpoint blockade, mice were gavaged with glycine, ornithine, or arginine daily for the two weeks after orthotopic tumor implantation, and on day 5, 9, and 13 after orthotopic tumor implantation mice were intraperitoneally injected with 200 µg of anti-PD-L1 monoclonal antibody (RMP1-14, BioXCell, BE0146, Lot: 810421D1) or isotype control (IgG2a, BioXCell, BE0089, Lot: 815021S1).

Fluorescence activated cell sorting

Tumors were processed into single cell suspensions via razor blade-mediated pulverization and enzymatic digestion with DNAse [200 mg/mL] (Sigma-Aldrich, 10104159001), Collagenase I [100 U/mL], and Collagenase Type IV [500 U/mL] (Worthington Biochemical, LS004197 and LS004189) on a shaking incubator (37 ºC) for 30 min. Enzymatic activity was quenched by doubling the volume of the tissue digest with FACS buffer (2% FCS in PBS). The resulting cell suspensions were filtered through 70 µm cell strainer (Corning, 352350) to obtain single cell suspensions. Lymph nodes and tumor-draining lymph nodes were pulverized with a 1 mL syringe plunger through a PBS wetted 70 µm cell strainer to generate single cell suspensions. For each sample, 5-10 x 10^6 cells were washed with PBS and stained with Zombie NIR Fixable live/dead dye (Biolegend, 423106) at 4 ºC for 20 min. Cells were washed with PBS followed by surface staining at 4 ºC with directly conjugated antibodies (see list below) diluted in FACS buffer containing anti-CD16/32 (BioXCell, BE0307, RRID:AB_2736987 or BioLegend, 101320, RRID:AB_1574975) for 30 min. Cells were washed again with FACS buffer. For intracellular staining, cells were fixed 4 ºC for 20 min and washed in permeabilization buffer from the Fix/Perm kit (BD Biosciences, 554714), Antibodies against intracellular targets were diluted in permeabilization buffer and cells were incubated at 4 ºC for 30 min followed by another wash prior to assessment with BD LSR Fortessa SORP cytometer. For T cell isolations, single cell suspensions were enriched for mononuclear cells using Ficoll-Paque Premium 1.084 (GE Healthcare, 17-5446-02). For isolation of myeloid cells, single cell tumor suspensions were enriched for $CD45^+$ cells using EasySep biotin positive selection kit (Stemcell Technologies, 17665). Enriched cells were stained at 4 ºC for 30 min with directly conjugated antibodies diluted in FACS buffer containing anti-CD16/32. Cells were washed with FACS buffer and filtered through 70 µm cell strainers. Immediately prior to sorting, DAPI was added to exclude dead cells. Cells were sorted on a BD FACSAria Fusion and BD FACSAria2. Sorted T cells were collected directly into RPMI (Gibco, 11875085) supplemented with 10% FCS (Benchmark, NC1643060), Pen/Strep/Glut (Gibco, 10378016), and b-mercaptoethanol [50 µM] (Gibco, 21985023) to be used for *ex vivo* stimulation assays with phorbol 12-myristate 12-acetate (PMA) [50 ng/mL] (Sigma, P8139), ionomycin [500 ng/mL] (Invitrogen, I24222), brefeldin A (BFA) [3 mg/mL] (Sigma, B7651) in 5% CO^2 at 37 ºC for 3-5 h. *Ex vivo* stimulated T cells were washed and stained for intracellular flow cytometric analysis as previously described.
All data generated with flow cytometry were generated and analyzed in a blinded fashion.

Antibody target – fluorophore (clone)	**Supplier**	**Catologue #; RRID**
anti-mouse Ly6C - BV711 (clone HK1.4)	Biolegend	Cat# 128037; RRID: AB_2562630

anti-mouse F4/80 - BV510 (clone BM8)	Biolegend	Cat# 123135; RRID: AB_2562622
anti-mouse CD24 - PECy7 (clone M1/69)	Biolegend	Cat# 101822; RRID: AB_756048
anti-mouse CD31 - AF647 (clone 390)	Biolegend	Cat# 102415; RRID: AB_493411
anti-mouse CD11c - BV650 (clone N418)	Biolegend	Cat# 117339: RRID: AB_2562414
anti-mouse CD11b - PerCp-Cy5.5 (clone ICRF44)	Biolegend	Cat# 301328: RRID: AB_10933428
anti-mouse I-A/I-E - PE (clone AF6-88.5)	Biolegend	Cat# 107630; RRID: AB_2069376
anti-mouse CD24 - BV421 (clone M1/69)	Biolegend	Cat# 101825; RRID: AB_10901159
anti-mouse CD31 - AF647 (clone 390)	Biolegend	Cat# 102415; RRID: AB_493411
anti-mouse CD38 - BV711 (clone 90/CD38)	BD BioSciences	Cat# 740697; RRID: AB_2740381
anti-mouse CD38 - FITC (clone 90/CD38)	BD BioSciences	Cat# 558813; RRID: AB_397126
anti-mouse CD4 - BUV395 (clone RM4-5)	BD BioSciences	Cat# 563790; RRID: AB_2738426
anti-mouse CD44 - BUV737 (clone IM7)	BD BioSciences	Cat# 564392; RRID: AB_2738785
anti-mouse CD44 - AF700 (clone IM7)	Thermo Fisher	Cat# 56-0441-80; RRID:AB_494012
anti-mouse CD45 AF647 (clone 30-F11)	Biolegend	Cat# 103124; RRID: AB_493533
anti-mouse CD45 - BUV395 (clone 30-F11)	BD BioSciences	Cat# 564279; RRID: AB_2651134
anti-mouse CD45 - BV421 (clone 30-F11)	Biolegend	Cat# 304032; RRID: AB_2561357
anti-mouse CD45.1 - BUV395 (clone A20)	BD BioSciences	Cat# 565212; RRID: AB_2722493
anti-mouse CD45.1 - PECy7 (clone A20)	Biolegend	Cat# 110730; RRID: AB_1134168
anti-mouse CD5 - BV510 (clone 53-7.3)	Biolegend	Cat# 100627; RRID: AB_2563930
anti-mouse CD69 - BV650 (clone H1.2F3)	Biolegend	Cat# 104541; RRID: AB_2616934
anti-mouse CD8 - AF488 (clone 53-6.7)	Biolegend	Cat# 100723; RRID: AB_389304
anti-mouse CD8 - PerCp-Cy5.5 (clone 53-6.7)	Biolegend	Cat# 100734; RRID: AB_2075238
anti-mouse H2kB - PE (clone AF6-88.5)	Biolegend	Cat# 116507; RRID: AB_313734
anti-mouse IFNy - PE (clone XMG1.2)	Thermo Fisher	Cat# 12-7311-81; RRID: AB_466192
anti-mouse IFNy - PECy7 (clone XMG1.2)	Biolegend	Cat# 505826; RRID: AB_2295770
anti-mouse Ki67 - PE eFluor610 (clone SolA15)	Thermo Fisher	Cat# 61-5698-82; RRID: AB_2574620
anti-mouse Ly6G - BV785 (clone 1A8)	Biolegend	Cat# 127645; RRID: AB_2566317
anti-mouse I-A/I-E - AF700 (clone M5/114.15.2)	Biolegend	Cat# 107622; RRID: AB_493727
anti-mouse PD-1 - BV605 (clone 29F.1A12)	Biolegend	Cat# 135219; RRID: AB_11125371
anti-mouse TCF1 - PE (clone S33-966)	BD BioSciences	Cat# 564217; RRID: AB_2687845
anti-mouse TNFa - BV421 (clone MP6-XT22)	Biolegend	Cat# 506327; RRID: AB_10900823
anti-mouse TNFa - PE (clone MP6-XT22)	Biolegend	Cat# 506306; RRID: AB_315427
anti-mouse TOX - APC (clone REA473)	Miltenyi Biotec	Cat# 130-118-335; RRID: AB_2751485

References

1. Mariathasan, S. *et al.* TGFβ attenuates tumour response to PD-L1 blockade by contributing to exclusion of T cells. *Nature 2018 554:7693* **554**, 544–548 (2018).

2. Tauriello, D. V. F. *et al.* TGFβ drives immune evasion in genetically reconstituted colon cancer metastasis. *Nature 2018 554:7693* **554**, 538–543 (2018).

3. Acerbi, I. *et al.* Human breast cancer invasion and aggression correlates with ECM stiffening and immune cell infiltration. *Integrative Biology* **7**, 1120–1134 (2015).

4. DeNardo, D. G. *et al.* Leukocyte complexity predicts breast cancer survival and functionally regulates response to chemotherapy. *Cancer Discov* **1**, 54–67 (2011).

5. Smyth, M. J., Ngiow, S. F., Ribas, A. & Teng, M. W. L. Combination cancer immunotherapies tailored to the tumour microenvironment. *Nature Reviews Clinical Oncology 2015 13:3* **13**, 143–158 (2015).

6. Binnewies, M. *et al.* Understanding the tumor immune microenvironment (TIME) for effective therapy. *Nature Medicine 2018 24:5* **24**, 541–550 (2018).

7. Maller, O. *et al.* Tumour-associated macrophages drive stromal cell-dependent collagen crosslinking and stiffening to promote breast cancer aggression. *Nature Materials 2020 20:4* **20**, 548–559 (2020).

8. Jiang, H., Hegde, S. & DeNardo, D. G. Tumor-associated fibrosis as a regulator of tumor immunity and response to immunotherapy. *Cancer Immunol Immunother* **66**, 1037–1048 (2017).

9. Broz, M. L. *et al.* Dissecting the tumor myeloid compartment reveals rare activating antigen-presenting cells critical for T cell immunity. *Cancer Cell* **26**, 638–652 (2014).

10. Movahedi, K. *et al.* Different tumor microenvironments contain functionally distinct subsets of macrophages derived from Ly6C(high) monocytes. *Cancer Res* **70**, 5728–5739 (2010).

11. Laviron, M. *et al.* Tumor-associated macrophage heterogeneity is driven by tissue territories in breast cancer. *Cell Rep* **39**, 110865 (2022).

12. Mujal, A. M. *et al.* Holistic Characterization of Tumor Monocyte-to-Macrophage Differentiation Integrates Distinct Immune Phenotypes in Kidney Cancer. *Cancer Immunology Research* **10**, 403–419 (2022).

13. Cassetta, L. *et al.* Human Tumor-Associated Macrophage and Monocyte Transcriptional Landscapes Reveal Cancer-Specific Reprogramming, Biomarkers, and Therapeutic Targets. *Cancer Cell* **35**, 588 (2019).

14. Wang, B. *et al.* Transition of tumor-associated macrophages from MHC class IIhito MHC class IIlowmediates tumor progression in mice. *BMC Immunology* **12**, 1–12 (2011).

15. Geeraerts, X. *et al.* Macrophages are metabolically heterogeneous within the tumor microenvironment. *Cell Rep* **37**, (2021).

16. Tharp, K. M. *et al.* Adhesion-mediated mechanosignaling forces mitohormesis. *Cell Metabolism* **33**, 1322-1341.e13 (2021).

17. Paszek, M. J. *et al.* Tensional homeostasis and the malignant phenotype. *Cancer Cell* **8**, 241–254 (2005).

18. Levental, K. R. *et al.* Matrix crosslinking forces tumor progression by enhancing integrin signaling. *Cell* **139**, 891–906 (2009).

19. Mouw, J. K. *et al.* Tissue mechanics modulate microRNA-dependent PTEN expression to regulate malignant progression. *Nat Med* **20**, 360 (2014).

20. Nicolas-Boluda, A. *et al.* Tumor stiffening reversion through collagen crosslinking inhibition improves t cell migration and anti-pd-1 treatment. *Elife* **10**, (2021).

21. Taufalele, P. v. *et al.* Matrix stiffness enhances cancer-macrophage interactions and M2-like macrophage accumulation in the breast tumor microenvironment. *Acta Biomaterialia* (2022) doi:10.1016/J.ACTBIO.2022.04.031.

22. Afik, R. *et al.* Tumor macrophages are pivotal constructors of tumor collagenous matrix. *Journal of Experimental Medicine* **213**, 2315–2331 (2016).

23. Schnoor, M. *et al.* Production of Type VI Collagen by Human Macrophages: A New Dimension in Macrophage Functional Heterogeneity. *The Journal of Immunology* **180**, 5707–5719 (2008).

24. Biochemistry of Collagens, Laminins and Elastin. *Biochemistry of Collagens, Laminins and Elastin* (2016) doi:10.1016/C2015-0-05547-2.

25. Noskovicova, N. *et al.* Suppression of the fibrotic encapsulation of silicone implants by inhibiting the mechanical activation of pro-fibrotic TGF-β. *Nature Biomedical Engineering 2021 5:12* **5**, 1437–1456 (2021).

26. Goswami, R. *et al.* Mechanosensing by TRPV4 mediates stiffness-induced foreign body response and giant cell formation. *Science Signaling* **14**, (2021).

27. Combes, A. J. *et al.* Discovering dominant tumor immune archetypes in a pan-cancer census. *Cell* **185**, 184-203.e19 (2022).

28. Sanin, D. E. *et al.* A common framework of monocyte-derived macrophage activation. *Science Immunology* **7**, (2022).

29. Yu, X. *et al.* The Cytokine TGF-β Promotes the Development and Homeostasis of Alveolar Macrophages. *Immunity* **47**, 903-912.e4 (2017).

30. Leight, J. L., Wozniak, M. A., Chen, S., Lynch, M. L. & Chen, C. S. Matrix rigidity regulates a switch between TGF-β1-induced apoptosis and epithelial-mesenchymal transition. *Molecular Biology of the Cell* **23**, 781–791 (2012).

31. Pang, Y. *et al.* TGF-β Signaling in myeloid cells is required for tumor metastasis. *Cancer Discovery* **3**, 936–951 (2013).

32. Geiger, R. *et al.* L-Arginine Modulates T Cell Metabolism and Enhances Survival and Anti-tumor Activity. *Cell* **167**, 829-842.e13 (2016).

33. Leone, R. D. & Powell, J. D. Metabolism of immune cells in cancer. *Nature Reviews Cancer 2020 20:9* **20**, 516–531 (2020).

34. Lim, A. R., Rathmell, W. K. & Rathmell, J. C. The tumor microenvironment as a metabolic barrier to effector T cells and immunotherapy. *Elife* **9**, 1–13 (2020).

35. Bantug, G. R., Galluzzi, L., Kroemer, G. & Hess, C. The spectrum of T cell metabolism in health and disease. *Nature Reviews Immunology* **18**, 19–34 (2018).

36. Rossiter, N. J. *et al.* CRISPR screens in physiologic medium reveal conditionally essential genes in human cells. *Cell Metabolism* **33**, 1248-1263.e9 (2021).

37. Leney-Greene, M. A., Boddapati, A. K., Su, H. C., Cantor, J. R. & Lenardo, M. J. Human Plasma-like Medium Improves T Lymphocyte Activation. *iScience* **23**, 100759 (2020).

38. Cantor, J. R. *et al.* Physiologic Medium Rewires Cellular Metabolism and Reveals Uric Acid as an Endogenous Inhibitor of UMP Synthase. *Cell* **169**, 258-272.e17 (2017).

39. Sullivan, M. R. *et al.* Quantification of microenvironmental metabolites in murine cancers reveals determinants of tumor nutrient availability. *Elife* **8**, (2019).

40. Kumar, V., Patel, S., Tcyganov, E. & Gabrilovich, D. I. The Nature of Myeloid-Derived Suppressor Cells in the Tumor Microenvironment. *Trends in Immunology* **37**, 208–220 (2016).

41. Raber, P., Ochoa, A. C. & Rodríguez, P. C. Metabolism of L-Arginine by Myeloid-Derived Suppressor Cells in Cancer: Mechanisms of T cell suppression and Therapeutic Perspectives. *http://dx.doi.org/10.3109/08820139.2012.680634* **41**, 614–634 (2012).

42. Caldwell, M. D., Mastrofrancesco, B., Shearer, J. & Bereiter, D. The temporal change in amino acid concentration within wound fluid--a putative rationale. *Prog Clin Biol Res* **365**, 205–222 (1991).

43. Albaugh, V. L., Mukherjee, K. & Barbul, A. Proline Precursors and Collagen Synthesis: Biochemical Challenges of Nutrient Supplementation and Wound Healing. *The Journal of Nutrition* **147**, 2011–2017 (2017).

44. Mehl, A. A., Damião, A. O. M. C., Viana, S. D. D. O. & Andretta, C. P. Hard-to-heal wounds: A randomised trial of an oral proline-containing supplement to aid repair. *Journal of Wound Care* **30**, 26–31 (2021).

45. Schwörer, S. *et al.* Proline biosynthesis is a vent for TGFβ-induced mitochondrial redox stress. *The EMBO Journal* **39**, e103334 (2020).

46. Durante, W., Liao, L., Reyna, S. v., Peyton, K. J. & Schafer, A. I. Transforming Growth Factor-β1 Stimulates l-Arginine Transport and Metabolism in Vascular Smooth Muscle Cells. *Circulation* **103**, 1121–1127 (2001).

47. Torrino, S. *et al.* Mechano-induced cell metabolism promotes microtubule glutamylation to force metastasis. *Cell Metabolism* **33**, 1342-1357.e10 (2021).

48. Guo, L. *et al.* Kindlin-2 links mechano-environment to proline synthesis and tumor growth. *Nature Communications 2019 10:1* **10**, 1–20 (2019).

49. Canale, F. P. *et al.* Metabolic modulation of tumours with engineered bacteria for immunotherapy. *Nature 2021 598:7882* **598**, 662–666 (2021).

50. Mak, T. W. *et al.* Glutathione Primes T Cell Metabolism for Inflammation. *Immunity* **46**, 675–689 (2017).

51. Yarosz, E. L. & Chang, C. H. The Role of Reactive Oxygen Species in Regulating T Cell-mediated Immunity and Disease. *Immune Network* **18**, (2018).

52. Engelhardt, J. J. *et al.* Marginating Dendritic Cells of the Tumor Microenvironment Cross-Present Tumor Antigens and Stably Engage Tumor-Specific T Cells. *Cancer Cell* **21**, 402–417 (2012).

53. Thompson, S. B. *et al.* Formin-like 1 mediates effector t cell trafficking to inflammatory sites to enable t cell-mediated autoimmunity. *Elife* **9**, 1–27 (2020).

54. Davidson, M. D., Burdick, J. A. & Wells, R. G. Engineered biomaterial platforms to study fibrosis. *Adv Healthc Mater* **9**, e1901682 (2020).

55. Carey, S. P., Martin, K. E. & Reinhart-King, C. A. Three-dimensional collagen matrix induces a mechanosensitive invasive epithelial phenotype. *Scientific Reports 2017 7:1* **7**, 1–14 (2017).

56. Riedel, S. *et al.* Design of biomimetic collagen matrices by reagent-free electron beam induced crosslinking: Structure-property relationships and cellular response. *Materials & Design* **168**, 107606 (2019).

57. Pakshir, P. *et al.* Dynamic fibroblast contractions attract remote macrophages in fibrillar collagen matrix. *Nature Communications* **10**, (2019).

58. Pickup, M. W., Mouw, J. K. & Weaver, V. M. The extracellular matrix modulates the hallmarks of cancer. *EMBO Rep* **15**, 1243–1253 (2014).

59. Simões, F. C. *et al.* Macrophages directly contribute collagen to scar formation during zebrafish heart regeneration and mouse heart repair. *Nature Communications 2020 11:1* **11**, 1–17 (2020).

60. Wishart, A. L. *et al.* Decellularized extracellular matrix scaffolds identify full-length collagen VI as a driver of breast cancer cell invasion in obesity and metastasis. *Science Advances* **6**, (2020).

61. Joyce, J. A. & Fearon, D. T. T cell exclusion, immune privilege, and the tumor microenvironment. *Science (1979)* **348**, 74–80 (2015).

62. Peranzoni, E. *et al.* Macrophages impede CD8 T cells from reaching tumor cells and limit the efficacy of anti–PD-1 treatment. *Proc Natl Acad Sci U S A* **115**, E4041–E4050 (2018).

63. Sun, L. *et al.* Activating a collaborative innate-adaptive immune response to control metastasis. *Cancer Cell* **39**, 1361-1374.e9 (2021).

64. Ganesh, K. & Massagué, J. TGF-β Inhibition and Immunotherapy: Checkmate. *Immunity* **48**, 626–628 (2018).

65. Tran, D. H. *et al.* Mitochondrial NADP+ is essential for proline biosynthesis during cell growth. *Nature Metabolism 2021 3:4* **3**, 571–585 (2021).

66. Adler, M. *et al.* Principles of Cell Circuits for Tissue Repair and Fibrosis. *iScience* **23**, 100841 (2020).

67. Nguyen-Chi, M. *et al.* Identification of polarized macrophage subsets in zebrafish. *Elife* **4**, (2015).

68. Foster, D. S., Jones, R. E., Ransom, R. C., Longaker, M. T. & Norton, J. A. The evolving relationship of wound healing and tumor stroma. *JCI Insight* **3**, (2018).

69. Timblin, G. A. *et al.* Mitohormesis reprogrammes macrophage metabolism to enforce tolerance. *Nature Metabolism 2021 3:5* **3**, 618–635 (2021).

70. Mills, C. D., Kincaid, K., Alt, J. M., Heilman, M. J. & Hill, A. M. M-1/M-2 Macrophages and the Th1/Th2 Paradigm. *The Journal of Immunology* **164**, 6166–6173 (2000).

71. van de Velde, L. A. *et al.* T Cells Encountering Myeloid Cells Programmed for Amino Acid-dependent Immunosuppression Use Rictor/mTORC2 Protein for Proliferative Checkpoint Decisions *. *Journal of Biological Chemistry* **292**, 15–30 (2017).

72. Eming, S. A., Murray, P. J. & Pearce, E. J. Metabolic orchestration of the wound healing response. *Cell Metabolism* **33**, 1726–1743 (2021).

73. Keshet, R., Szlosarek, P., Carracedo, A. & Erez, A. Rewiring urea cycle metabolism in cancer to support anabolism. *Nature Reviews Cancer 2018 18:10* **18**, 634–645 (2018).

74. Poolman, B., Driessen, A. J. M. & Konings, W. N. Regulation of arginine-ornithine exchange and the arginine deiminase pathway in Streptococcus lactis. *Journal of Bacteriology* **169**, 5597–5604 (1987).

75. Li, S. *et al.* Metabolism drives macrophage heterogeneity in the tumor microenvironment. *Cell Reports* **39**, 110609 (2022).

76. Dröge, W. *et al.* Suppression of cytotoxic T lymphocyte activation by L-ornithine. *The Journal of Immunology* **134**, (1985).

77. Lercher, A. *et al.* Type I Interferon Signaling Disrupts the Hepatic Urea Cycle and Alters Systemic Metabolism to Suppress T Cell Function. *Immunity* **51**, 1074 (2019).

78. Wouters, O. Y., Ploeger, D. T. A., van Putten, S. M. & Bank, R. A. 3,4-Dihydroxy-L-Phenylalanine as a Novel Covalent Linker of Extracellular Matrix Proteins to Polyacrylamide Hydrogels with a Tunable Stiffness. *Tissue Eng Part C Methods* **22**, 91–101 (2016).

79. Kaukonen, R., Jacquemet, G., Hamidi, H. & Ivaska, J. Cell-derived matrices for studying cell proliferation and directional migration in a complex 3D microenvironment. *Nature Protocols 2017 12:11* **12**, 2376–2390 (2017).

80. Tharp, K. M. *et al.* Actomyosin-Mediated Tension Orchestrates Uncoupled Respiration in Adipose Tissues. *Cell Metab* **27**, 602-615.e4 (2018).

81. Dobin, A. *et al.* STAR: ultrafast universal RNA-seq aligner. *Bioinformatics* **29**, 15–21 (2013).

82. Lin, Y. C. *et al.* A global network of transcription factors, involving E2A, EBF1 and Foxo1, that orchestrates B cell fate. *Nat Immunol* **11**, 635–643 (2010).

83. Eisen, M. B., Spellman, P. T., Brown, P. O. & Botstein, D. Cluster analysis and display of genome-wide expression patterns. *Proc Natl Acad Sci U S A* **95**, 14863–14868 (1998).

84. Zhou, Y. *et al.* Metascape provides a biologist-oriented resource for the analysis of systems-level datasets. *Nat Commun* **10**, 1523 (2019).

85. Robinson, M. D. & Oshlack, A. A scaling normalization method for differential expression analysis of RNA-seq data. *Genome Biology* **11**, 1–9 (2010).

86. Cameron, A. M. *et al.* Inflammatory macrophage dependence on NAD(+) salvage is a consequence of reactive oxygen species-mediated DNA damage. *Nat Immunol* **20**, 420–432 (2019).

87. Abe, M. *et al.* An assay for transforming growth factor-beta using cells transfected with a plasminogen activator inhibitor-1 promoter-luciferase construct. *Anal Biochem* **216**, 276–284 (1994).

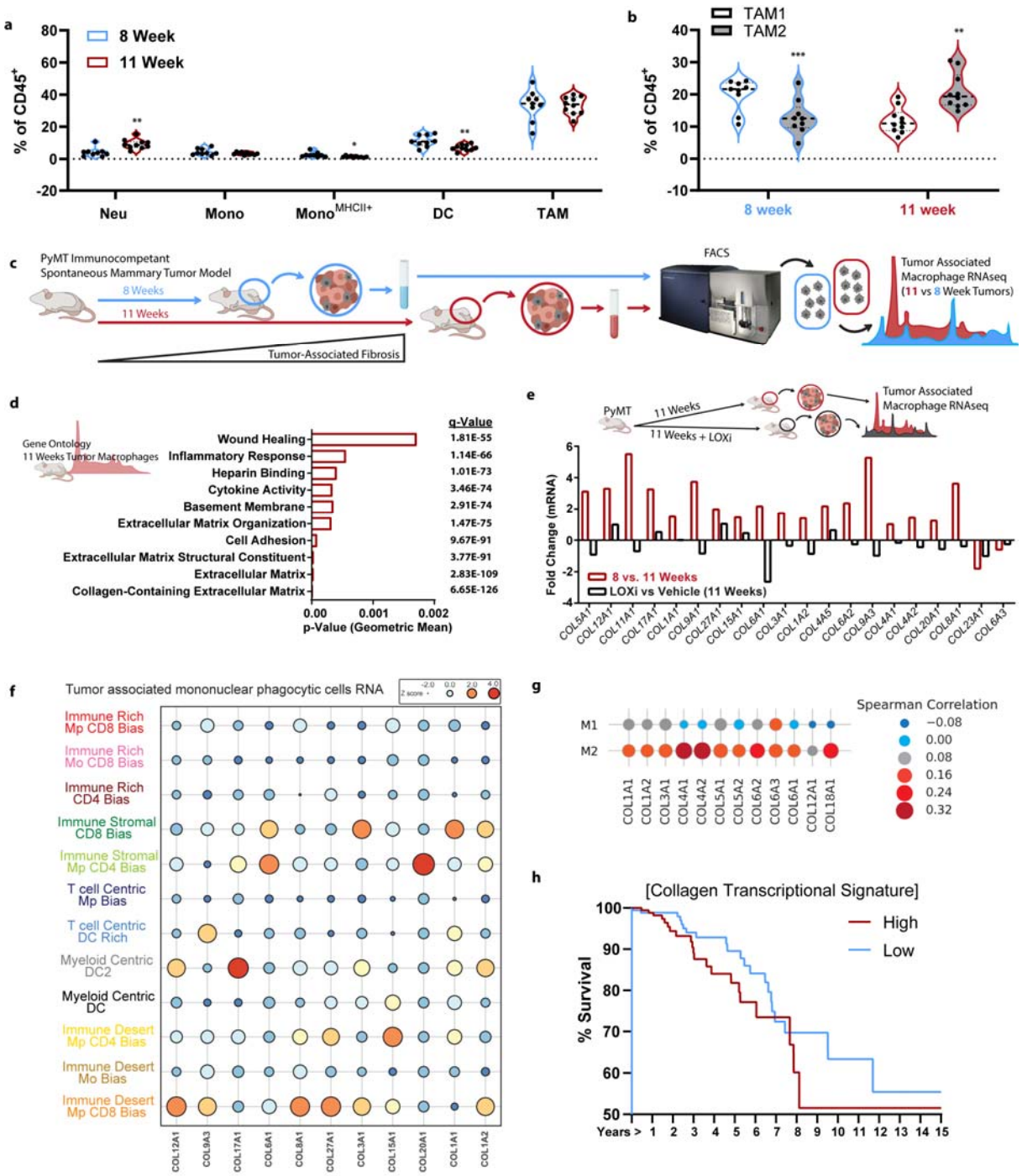

Figure 1:

a. Quantification of tumor infiltrating CD45$^+$ cell types, PyMT mammary tumors from 8 or 11-week old C57BL6/J mice, FACS gating strategy (Fig s.x), (n=9).

b. Quantitation of the percentage of TAM1 vs TAM2 of tumor infiltrating CD45$^+$ cell types, PyMT mammary tumors from 8 or 11 week old C57BL6/J mice, (n=9).

c. Graphical representation of experimental setup for (d).

d. Gene Ontology (GO) enriched in TAMs derived from 11 week old PyMT mammary tumors relative to TAMs derived from 8 week old PyMT mammary tumors, (n=5).

e. Relative gene expression comparing the top GO category identified in d for TAMs derived from 11 week old PyMT mammary tumors treated with or without LOX-inhibition (LOXi) in the drinking water (~3 mg/kg/day), (n=5).

f. Bubble plot of collagen gene expression of the tumor associated myeloid compartment from the Immunoprofiler cohort (IPI) containing 12 different solid tumor types, grouped by cluster/archetype identified in the IPI cohort [27].

g. Spearman rank correlation of the gene set variation analysis of the top GO category identified in d and macrophage polarization signatures of tumor transcriptomes collected from the TCGA repository (TCGA projects: pancreatic adenocarcinoma, lung adenocarcinoma, glioblastoma multiforme, breast invasive carcinoma, kidney renal clear cell carcinoma).

h. Kaplan-Meier survival curves of 2506 stage II and IIIA breast tumors, stratified for the top and bottom quartile expression level of the genes comprising the top GO category identified in d.

*Data shown represent ± SEM. *P < 0.05, **P < 0.01, or ***P < 0.005 via two-tailed unpaired Student t test (a-b).*

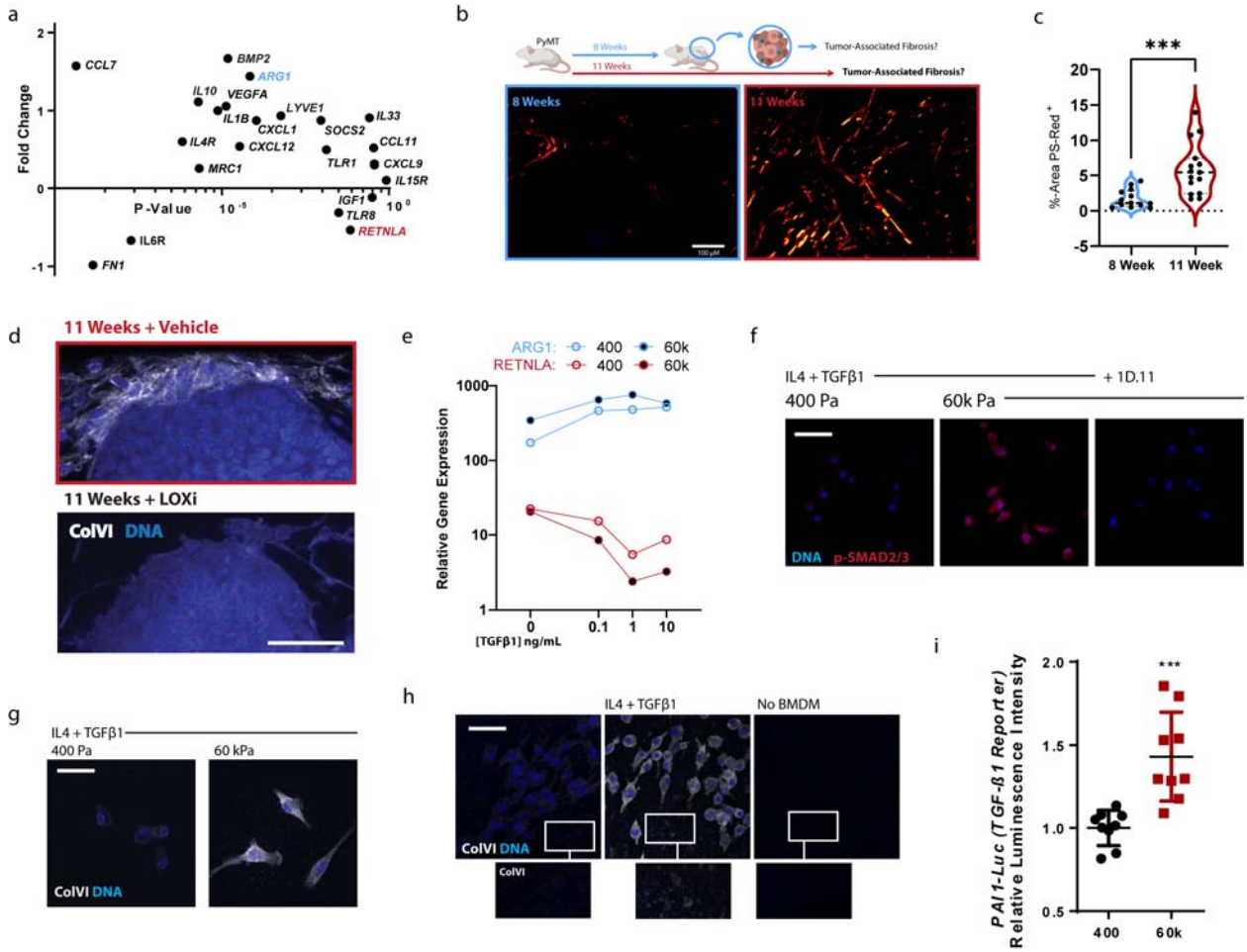

Figure S1:

a. Relative expression of macrophage polarization-associated gene expression of TAMs derived from 11 week old PyMT mammary tumors, relative to TAMs derived from 8 week old PyMT mammary tumors, (n=5).

b. Representative birefringence of collagen fibers via polarized light microscopy of picrosirius red (PS-red) stained 8 and 11 week old PyMT mammary tumors, (scale bar: 100 µm).

c.% area of PyMT tumor determined to be fibular collagen with picrosirius red (PS-red) staining (n=13 or 15).

d. Representative immunofluorescence microscopy of Collagen VI (white) and DNA (blue) of 11 week old PyMT mammary tumors treated with or without LOX-inhibition, (Scale Bar: 100 µm).

e. Relative gene expression of IL4-polarized BMDMs cultured on soft (400 Pa) or stiff (60k Pa) collagen I-coated polyacrylamide hydrogel surfaces treated with 0, 0.1, 1, or 10 ng/mL TGFβ1 for 4 h, qPCR-ΔΔCT normalized to BMDMs treated without IL4 (housekeeping gene: 18s), (n=3).

f. Representative immunofluorescence microscopy for phosphorylated-SMAD2/3 (red) and DNA (blue) of IL4-polarized BMDMs cultured on soft (400 Pa) or stiff (60k Pa) collagen I-coated

polyacrylamide hydrogel surfaces, treated with 1 ng/mL TGFβ1 with or without 10 µg/mL TGFβ1-blocking antibody (1D.11) for 24 h, (scale bar: 40 µm).

g. Representative immunofluorescence microscopy of Collagen VI (white) and DNA (blue) of IL4-polarized BMDMs cultured on soft (400 Pa) or stiff (60k Pa) collagen I-coated polyacrylamide hydrogel surfaces treated with 1 ng/mL TGFβ1 for 24 h, (scale bar: 20 µm).

h. Representative immunofluorescence microscopy of Collagen VI (white) and DNA (blue) of BMDMs treated with or without 5 ng/mL IL4 and 1 ng/mL TGFβ1 on fibroblast synthesized ECM surfaces for 24 h, (scale bar: 40 µm).

i. Relative luminescent intensity of TGFβ1-reporter (PAI-1 Luc) expressing mink lung epithelial cells [87] when cultured for 24h in 1:1 conditioned media from IL4-polarized BMDMs cultured on soft (400 Pa) or stiff (60k Pa), (n=9).

*Data shown represent ± SEM. ***P < 0.005 via two-tailed unpaired Student t test (c and h).*

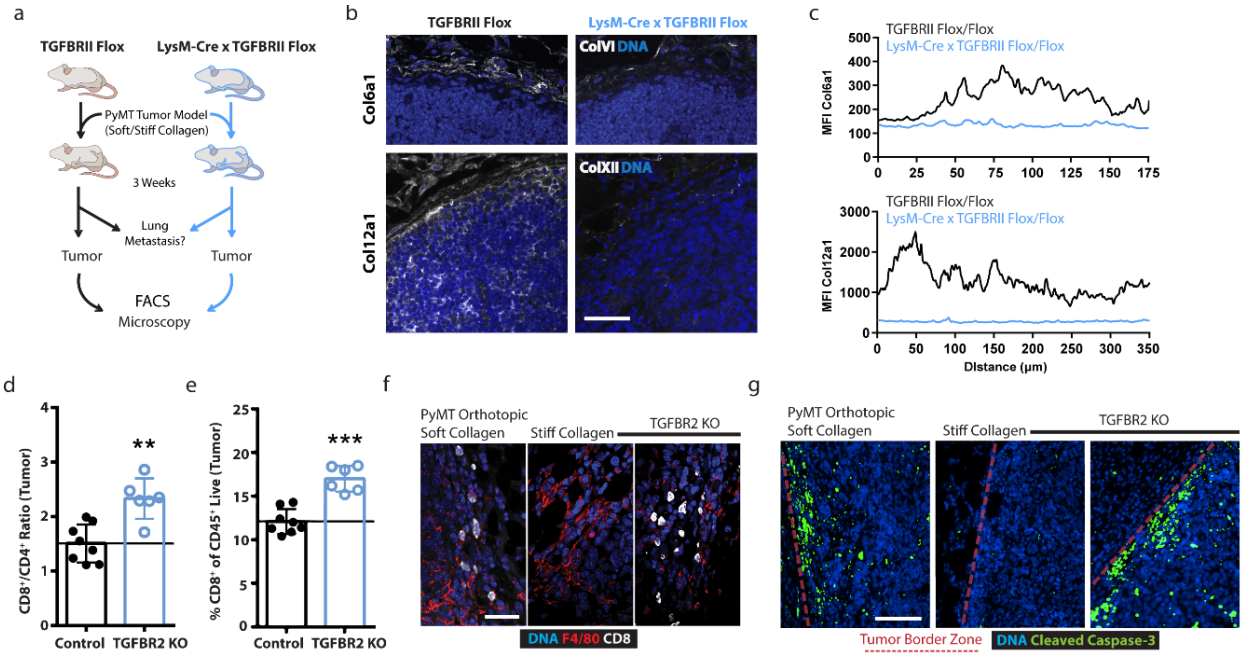

Figure 2:

a. Graphical representation of experimental setup for (b-g).

b. Representative immunofluorescence microscopy of Collagen VI (white) and DNA (blue) of orthotopic PyMT mammary after 3 weeks of growth in TGFβRII^{MyeKO} or control animals (Scale Bar: 100 µm).

c. Quantitation of immunofluorescence microscopy of Collagen VI or XII (white) and DNA (blue) of orthotopic PyMT mammary after 3 weeks of growth in TGFβRII^{MyeKO} or control animals, trace represents the MFI of Collagen VI or XII across 4 transverse sections of the tumor-stromal border (starting ~50 µm into the stroma and 125-300 µm into the tumor), (n=5).

d. Ratio of tumor infiltrating CD8^{+} to CD4^{+} cell types in stiff collagen orthotopic PyMT mammary after 3 weeks of growth in TGFβRII^{MyeKO} or control animals, FACS gating strategy (Fig. s.xyz), (n=8 or 6).

e. Quantification of tumor infiltrating CD8^{+} cells as a percentage of CD45^{+} cells found in stiff collagen orthotopic PyMT mammary after 3 weeks of growth in TGFβRII^{MyeKO} or control animals, FACS gating strategy (Fig. s.xyz), (n=8 or 6).

f. Representative immunofluorescence microscopy of CD8 (white), F4/80 (red), and DNA (blue) of soft or stiff collagen orthotopic PyMT mammary after 3 weeks of growth in TGFβRII^{MyeKO} or control animals (Scale Bar: 40 µm).

g. Representative immunofluorescence microscopy of cleaved-caspase 3 (red), and DNA (blue) of soft or stiff collagen orthotopic PyMT mammary after 3 weeks of growth in TGFβRII^{MyeKO} or control animals (Scale Bar: 100 µm).

*Data shown represent ± SEM. **P < 0.01 or ***P < 0.005 via two-tailed unpaired Student t test (d-f).*

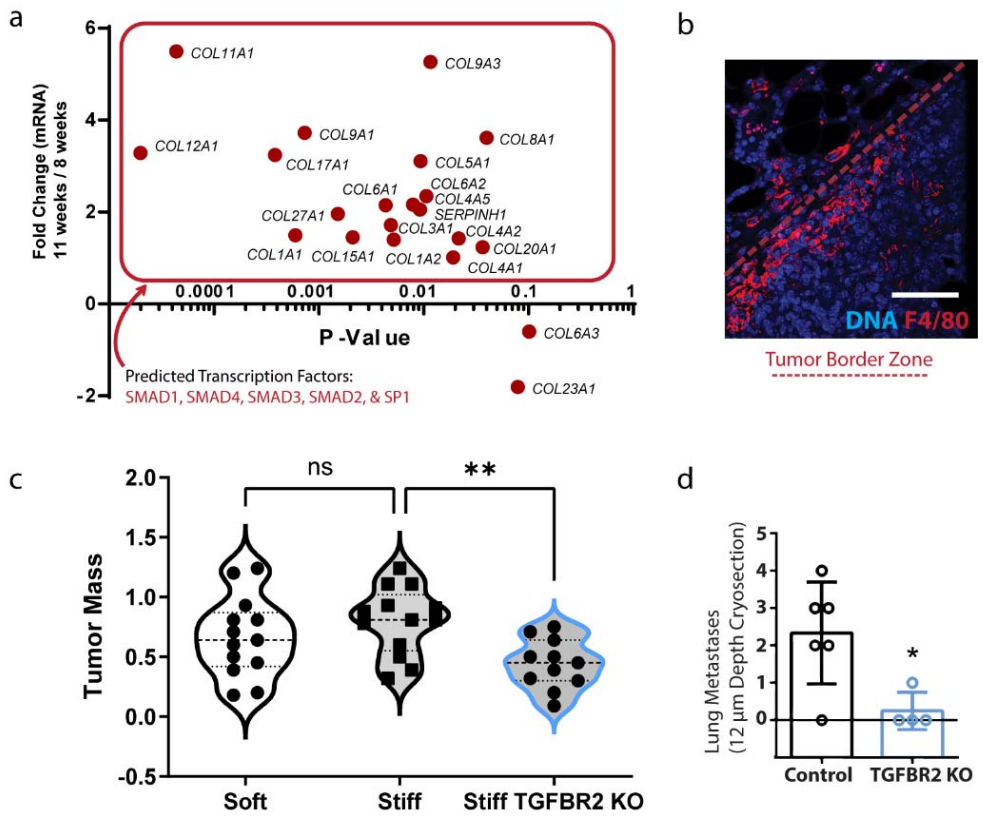

Figure S2:

a. XY-plot of relative genes comprising the GO category (collagen-containing ECM) in TAMs derived from 11 week old PyMT mammary tumors relative to TAMs derived from 8 week old PyMT mammary tumors, TRRUST transcription factor enrichment analysis: p-value SAMD1 10^{-6} and SP1 $10^{-2.8}$, combined Scores: SMAD1 (127.699827), SMAD4 (90.48497202), SMAD3 (48.37819162), SMAD2 (46.66904886), and SP1 (6.551517203).

b. Representative immunofluorescence microscopy of F4/80 (red) and DNA (blue) in 11 week old PyMT mammary tumors (Scale Bar: 40 µm).

c. Quantification of tumor masses accumulated after 3 weeks of in vivo growth of soft or stiff collagen orthotopic PyMT mammary tumors in TGFβRII^{MyeKO} or control animals, (n=13 or 11).

d. Quantification of lung metastasis via immunofluorescence microscopy of PyMT staining in lungs of 11 week old spontaneous PyMT mammary tumors TGFβRII^{MyeKO} or control animals (FVB/NJ), (n = 6 or 4)

*Data shown represent ± SEM. **P < 0.01 via one-way ANOVA with Tukey test for multiple comparisons (c) and *P < 0.05 via two-tailed unpaired Student t test (d).*

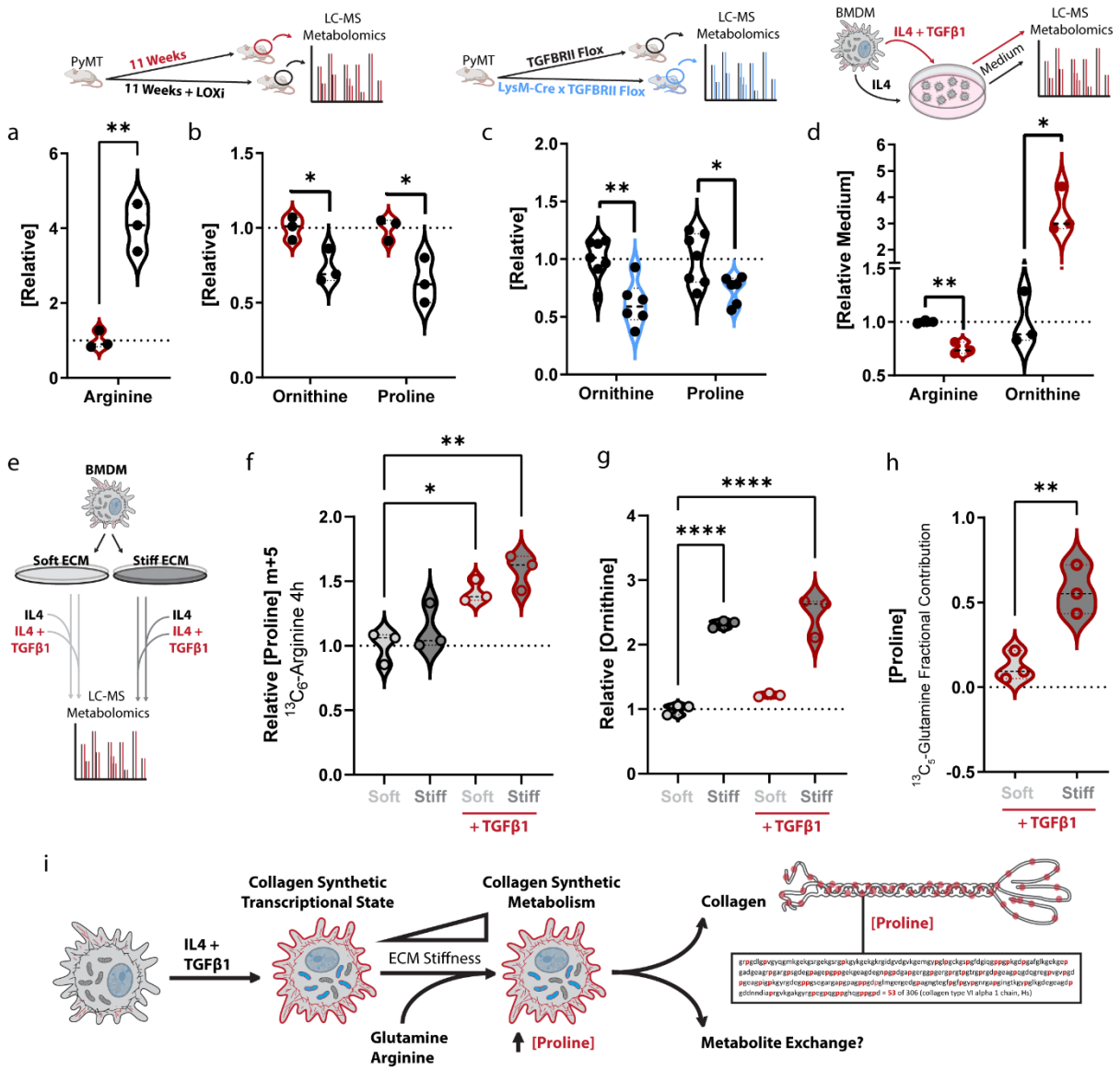

Figure 3:

a. Relative arginine concentration of 11 week old PyMT mammary tumors treated with or without LOX-inhibition (LOXi) in the drinking water (~3 mg/kg/day), LC-MS analysis, (n=3).

b. Relative ornithine and proline concentrations of 11 week old PyMT mammary tumors treated with or without LOX-inhibition (LOXi) in the drinking water (~3 mg/kg/day, LC-MS analysis, (n=3).

c. Relative ornithine and proline concentrations of stiff collagen orthotopic PyMT mammary tumors in TGFβRII^{MyeKO} or control animals for 3 weeks, LC-MS analysis, (n=7 or 6).

d. Relative medium concentrations of arginine and ornithine from culture with IL4-polarized BMDMs treated with or without 1 ng/mL TGFβ1 for 22 h, swapped for fresh medium for 2 h which was measured via LC-MS analysis, (n=3).

e. Graphical representation of experimental setup for (f-g).

f. ^{13}C tracing of $^{13}C_6$-arginine metabolism into $^{13}C_5$-proline in BMDMs cultured on soft (400 Pa) or stiff (60k Pa) collagen I-coated polyacrylamide hydrogel surfaces in medium containing $^{12}C_6$-arginine, treated with or without 1 ng/mL TGFβ1 for 20 h, swapped for fresh medium containing $^{13}C_6$-arginine for 4 h, BMDMs were harvested and measured via LC-MS, (n=3).

g. Relative ornithine concentration in BMDMs cultured on soft (400 Pa) or stiff (60k Pa) collagen I-coated polyacrylamide hydrogel surfaces with or without 1 ng/mL TGFβ1 for 24 h, measured via LC-MS, (n=3).

h. Fractional contributions (i.e., all isotopologues) of ^{13}C derived from $^{13}C_5$-glutamine in BMDMs cultured on soft (400 Pa) or stiff (60k Pa) collagen I-coated polyacrylamide hydrogel surfaces in medium containing $^{12}C_5$-glutamine, treated with or without 1 ng/mL TGFβ1 for 22 h, swapped for fresh medium containing $^{13}C_5$-glutamine for 2 h, BMDMs were harvested and measured via LC-MS, (n=3).

i. Graphical depiction of the observed relationship between TGFβ1 signaling and ECM stiffness in the context of collagen synthesis and proline metabolism.

*Data shown represent ± SEM. *P < 0.05 and **P < 0.01 via two-tailed unpaired Student t test (a-d) and *P < 0.05, **P < 0.01, or ****P < 0.0001 via one-way ANOVA with Tukey test for multiple comparisons (f-h).*

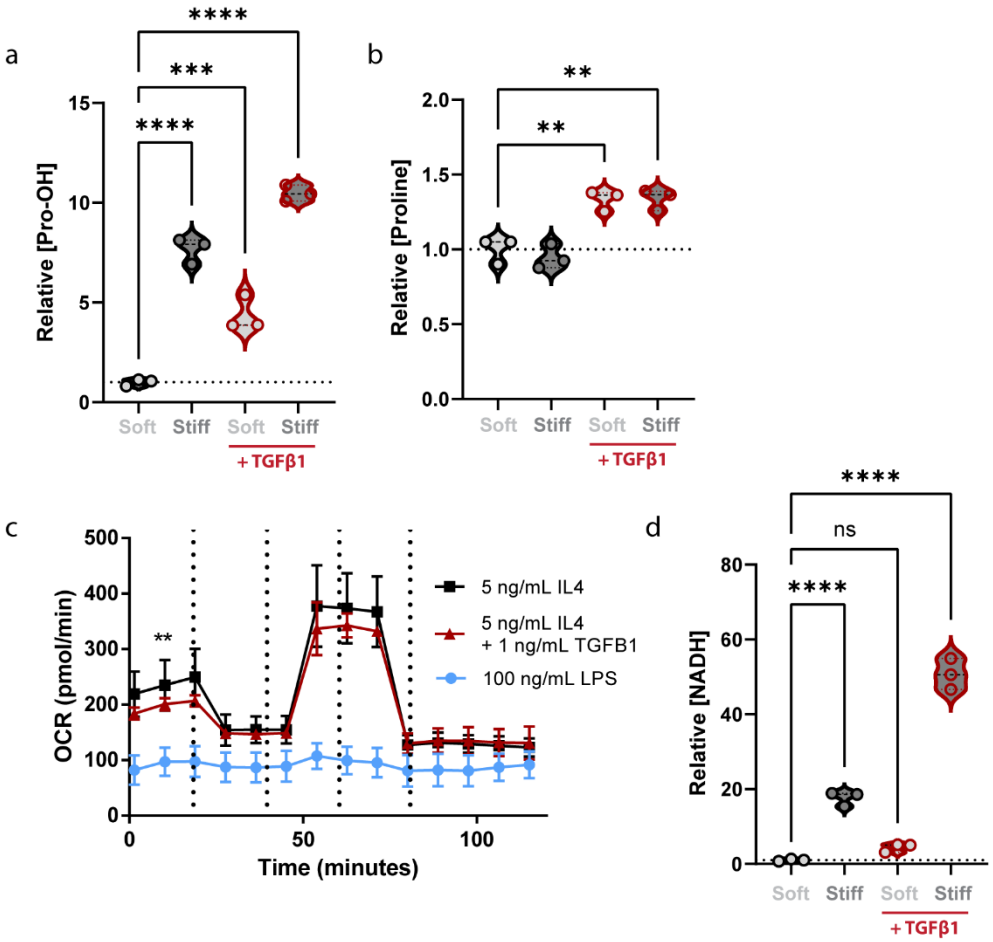

Figure S3:

a. Relative hydroxyproline (Pro-OH) concentration in BMDMs cultured on soft (400 Pa) or stiff (60k Pa) collagen I-coated polyacrylamide hydrogel surfaces with or without 1 ng/mL TGFβ1 for 24 h, measured via LC-MS, (n=3).

b. Relative proline concentration in BMDMs cultured on soft (400 Pa) or stiff (60k Pa) collagen I-coated polyacrylamide hydrogel surfaces with or without 1 ng/mL TGFβ1 for 24 h, measured via LC-MS, (n=3).

c. Cellular respirometry of BMDMs cultured with or without 1 ng/mL TGFβ1 for 24h or 100 ng/mL LPS for 1 h along with sequential additions via injection ports of Oligomycin [1 µM final], FCCP [1 µM final], and Antimycin A/Rotenone [1 µM final] during respirometry measurements, measured with an SeahorseXF24, (n=5 wells, repeated 3 times)

d. Relative NADH concentration in BMDMs cultured on soft (400 Pa) or stiff (60k Pa) collagen I-coated polyacrylamide hydrogel surfaces with or without 1 ng/mL TGFβ1 for 24 h, measured via LC-MS, (n=3).

*Data shown represent ± SEM. **P < 0.01 or ****P < 0.0001 via one-way ANOVA with Tukey test for multiple comparisons (a, b, and d) and **P < 0.01 via two-tailed unpaired Student t test (c), ns indicates statistically not significant.*

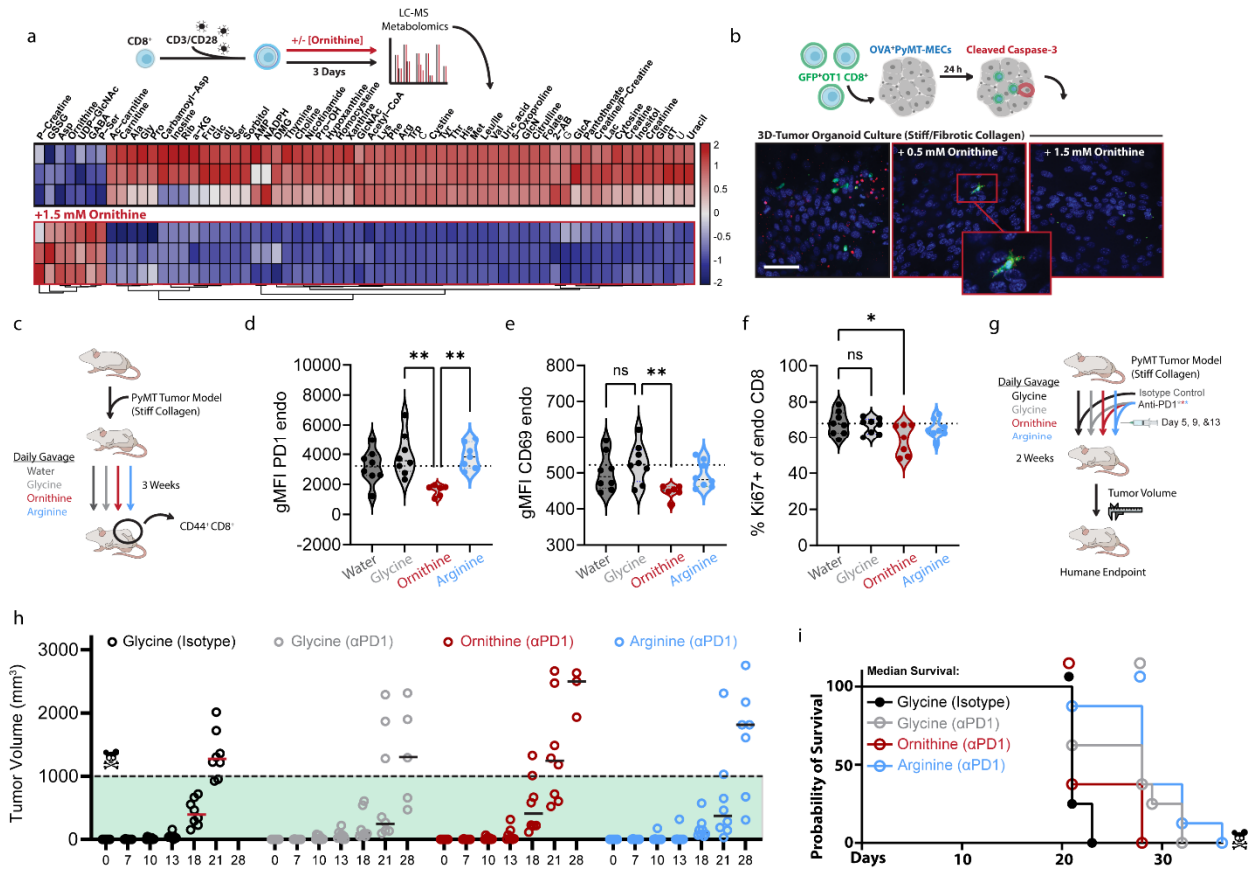

Figure 4:

a. Heat map of relative metabolite levels of CD3/CD28-activated CD8$^+$ CTLs cultured for 72 h in medium containing a molar ratio of 3:1 ornithine:arginine, medium refreshed every 24 h, LC-MS analysis. (n=3 biological replicates)

b. Representative immunofluorescence microscopy of stiff-collagen OVA-PyMT tumor organoids challenged with GFP$^+$-OTI CTLs (green) for 24 h in medium containing a molar ratio of 1:1 [0.5mM] or 3:1 [1.5 mM] ornithine:arginine, cleaved-caspase 3 (red) and DNA (blue), (Scale Bar: 40 µm).

c. Graphical description of the experimental setup for d-f.

d. Mean fluorescent intensity of PD1 staining of endogenous CD8$^+$ CTLs isolated from stiff collagen PyMT tumors after 3 weeks of growth in C57BL6/J mice gavaged daily with 2 g/kg glycine, ornithine, arginine, or water (100 µL), (n=8).

e. Mean fluorescent intensity of CD69 staining of endogenous CD8$^+$ CTLs isolated from stiff collagen PyMT tumors after 3 weeks of growth in C57BL6/J mice gavaged daily with 2 g/kg glycine, ornithine, arginine, or water (100 µL), (n=8).

f. Quantification of KI67 incorporation into endogenous CD8$^+$ CTLs isolated from stiff collagen PyMT tumors after 3 weeks of growth in C57BL6/J mice gavaged daily with 2 g/kg glycine, ornithine, arginine, or water (100 µL) and stimulated ex vivo with PMA [50 ng/mL] and ionomycin [500 ng/mL], (n=8).

g. Graphical description of the experimental setup for h-i.

h. Tumor volume measurements of stiff collagen PyMT tumors over 4 weeks of growth in C57BL6/J mice gavaged daily with 2 g/kg glycine, ornithine, or arginine (100 µL) for the first 14 days and treated with isotype control or anti-PD1 blocking antibodies on day 5, 9, and 13, humane endpoint indicated by horizontal dotted line and white background (n=8)

i. Kaplan-Meier survival curves of stage of experiment depicted in h. Mean survival of glycine treated isotype control and ornithine treated anti-PD1: 21 days, Mean survival of glycine and arginine treated anti-PD1: 28 days.

*Data shown represent ± SEM. *P < 0.05 or **P < 0.01 via one-way ANOVA with Tukey test for multiple comparisons (d-f).*

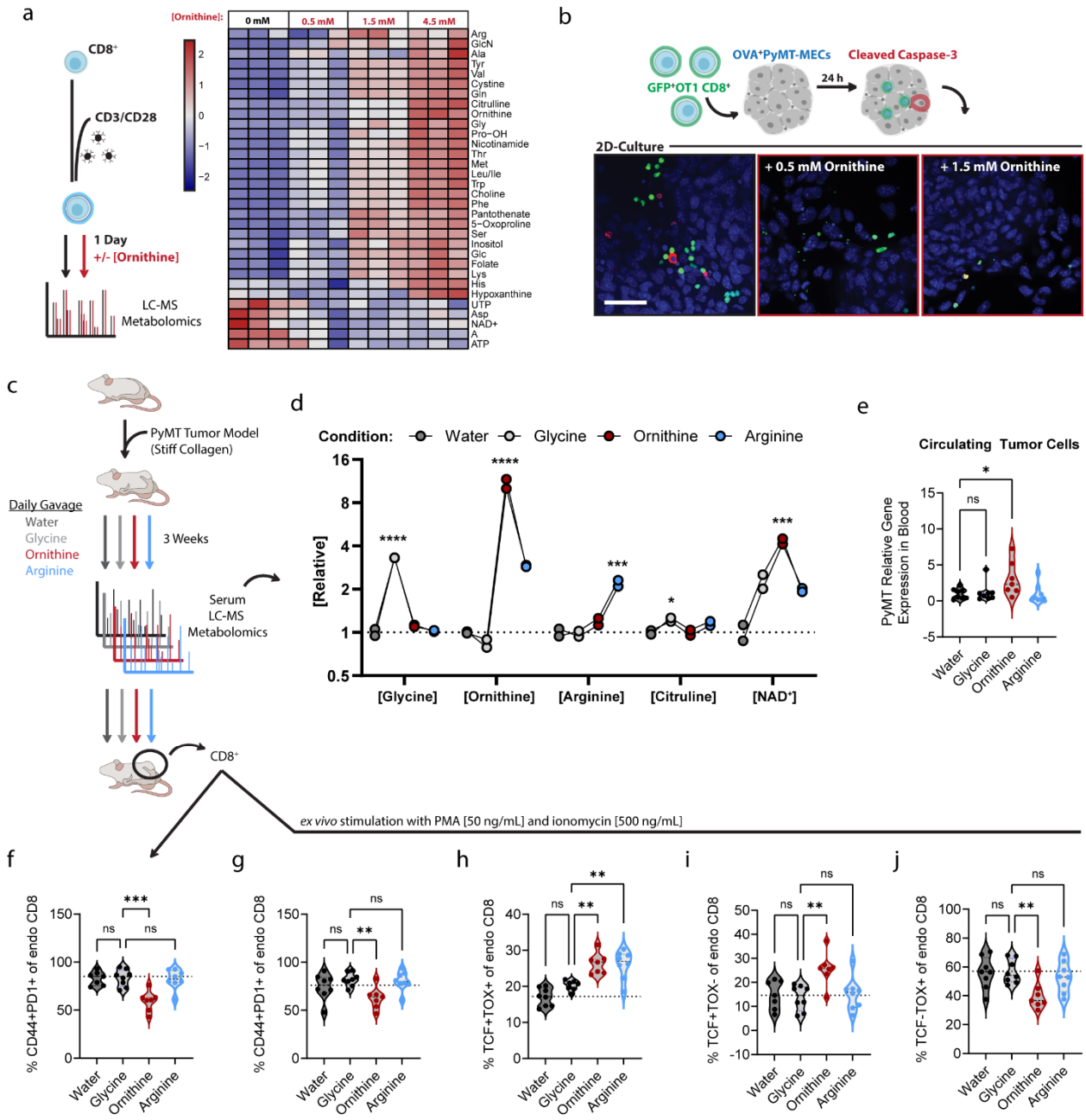

Figure S4:

a. Heat map of relative metabolite levels of CD3/CD28-activated CD8$^+$ CTLs cultured for 24 h in medium containing a molar ratio of 1:1 [0.5 mM], 3:1 [1.5 mM], and 9:1 [4.5 mM] ornithine:arginine, LC-MS analysis. (n=3 biological replicates)

b. Representative immunofluorescence microscopy of OVA-PyMT tumor cells challenged with GFP$^+$-OTI CTLs (green) for 24 h in medium containing a molar ratio of 1:1 [0.5mM] or 3:1 [1.5 mM] ornithine:arginine, cleaved-caspase 3 (red) and DNA (blue), (Scale Bar: 40 µm).

c. Graphical description of the experimental setup for d-j.

d. Relative serum metabolites derived from retro-orbital isolated blood from mice containing PyMT tumors after 3 weeks of growth in C57BL6/J mice gavaged daily with 2 g/kg glycine, ornithine, arginine, or water (100 µL), 4 h prior to isolation of blood/serum, measured with LC-MS (n=8 pooled into two technical replicates).

e. qPCR based assessment of circulating tumor cells via PyMT expression in blood clot isolated from blood collected for serum metabolite analysis (e), qPCR-ΔΔCT (housekeeping gene: 18s), (n=8).

f. Percentage of $PD1^+$ endogenous $CD8^+$ CTLs isolated from stiff collagen PyMT tumors after 3 weeks of growth in C57BL6/J mice gavaged daily with 2 g/kg glycine, ornithine, arginine, or water (100 µL), (n=8).

g. Percentage of $CD44^+$ endogenous $CD8^+$ CTLs isolated from stiff collagen PyMT tumors after 3 weeks of growth in C57BL6/J mice gavaged daily with 2 g/kg glycine, ornithine, arginine, or water (100 µL), (n=8).

h-j Quantification of TCF and TOX in endogenous $CD8^+$ CTLs isolated from stiff collagen PyMT tumors after 3 weeks of growth in C57BL6/J mice gavaged daily with 2 g/kg glycine, ornithine, arginine, or water (100 µL) and stimulated ex vivo with PMA [50 ng/mL] and ionomycin [500 ng/mL], (n=8).

*Data shown represent ± SEM. *P < 0.05, **P < 0.01, ***P < 0.005, or ****P < 0.001 via one-way ANOVA with Tukey test for multiple comparisons (d-j).*

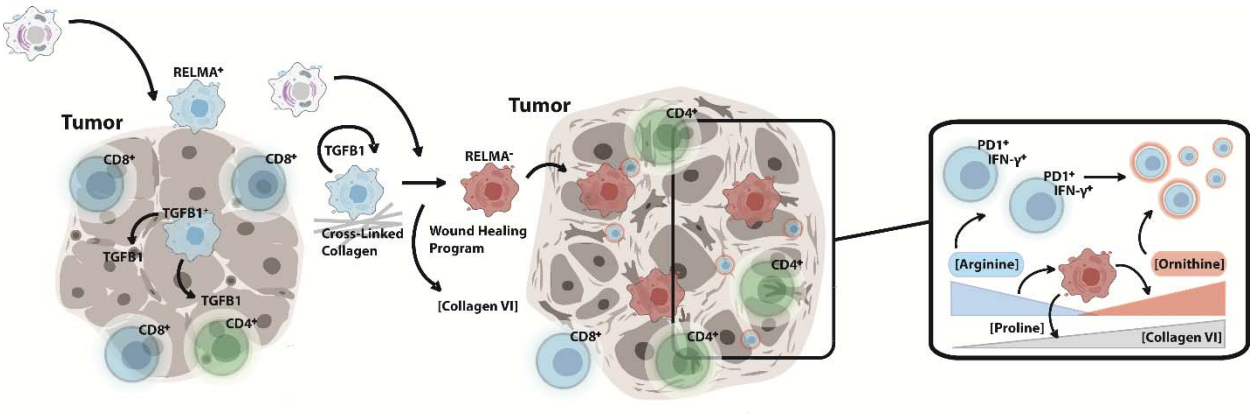

Figure 5:

Graphical representation of the identified relationship between the TME, infiltrating myeloid cells, mechano-metabolic programming, and CTLs in the TME.

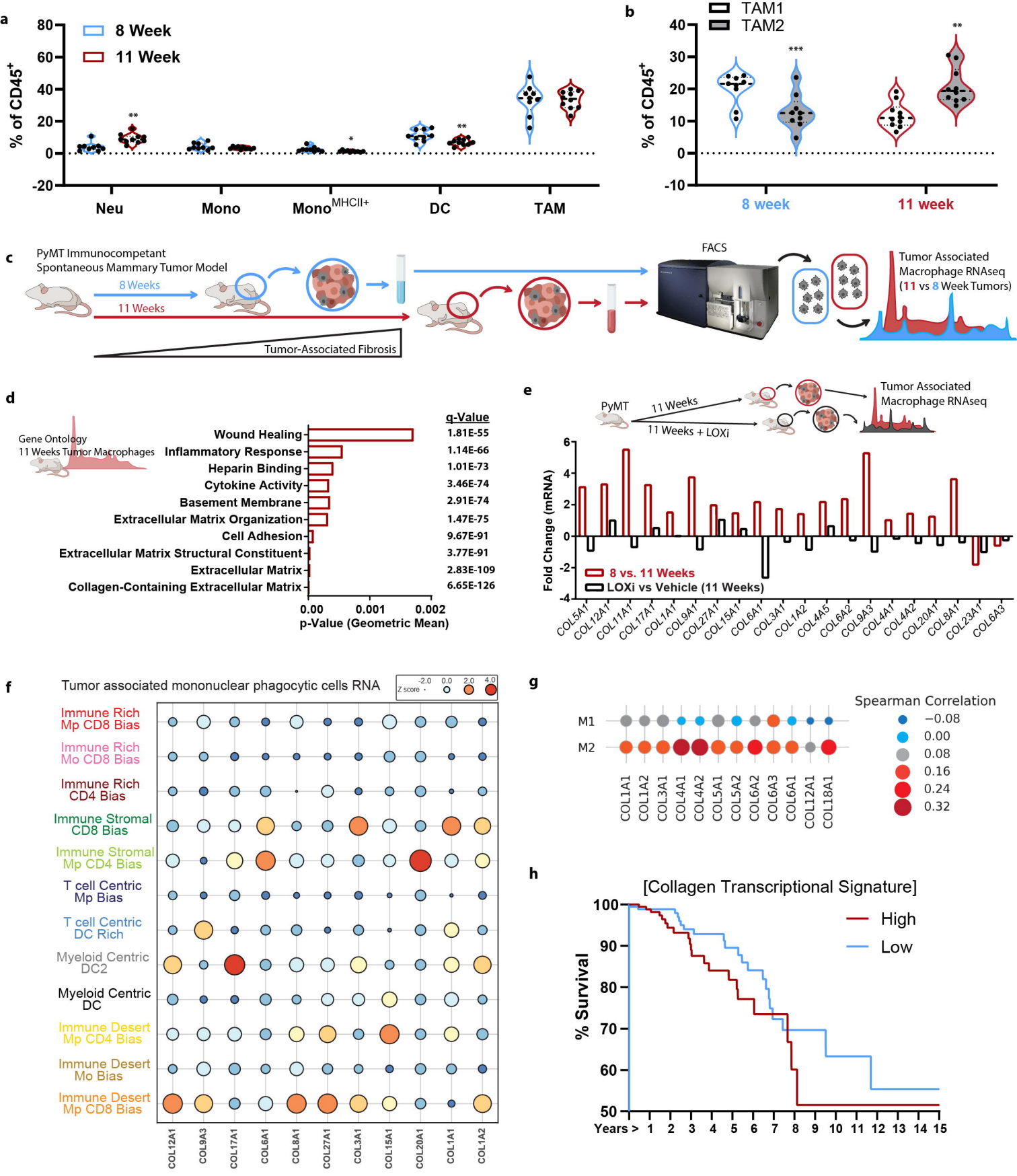
a
8 Week
11 Week
% of CD45+
Neu
Mono
Mono MHCII+
DC
TAM
b
TAM1
TAM2
% of CD45+
8 week
11 week
c
PyMT Immunocompetant
Spontaneous Mammary Tumor Model
8 Weeks
11 Weeks
Tumor-Associated Fibrosis
FACS
Tumor Associated
Macrophage RNAseq
(11 vs 8 Week Tumors)
d
Gene Ontology
11 Weeks Tumor Macrophages
q-Value
Wound Healing 1.81E-55
Inflammatory Response 1.14E-66
Heparin Binding 1.01E-73
Cytokine Activity 3.46E-74
Basement Membrane 2.91E-74
Extracellular Matrix Organization 1.47E-75
Cell Adhesion 9.67E-91
Extracellular Matrix Structural Constituent 3.77E-91
Extracellular Matrix 2.83E-109
Collagen-Containing Extracellular Matrix 6.65E-126
p-Value (Geometric Mean)
e
PyMT
11 Weeks
11 Weeks + LOXi
Tumor Associated
Macrophage RNAseq
Fold Change (mRNA)
8 vs. 11 Weeks
LOXi vs Vehicle (11 Weeks)
COL5A1
COL12A1
COL11A1
COL17A1
COL1A1
COL9A1
COL27A1
COL15A1
COL6A1
COL3A1
COL1A2
COL4A5
COL6A2
COL9A3
COL4A1
COL4A2
COL20A1
COL8A1
COL23A1
COL6A3
f
Tumor associated mononuclear phagocytic cells RNA
Z score
Immune Rich Mp CD8 Bias
Immune Rich Mo CD8 Bias
Immune Rich CD4 Bias
Immune Stromal CD8 Bias
Immune Stromal Mp CD4 Bias
T cell Centric Mp Bias
T cell Centric DC Rich
Myeloid Centric DC2
Myeloid Centric DC
Immune Desert Mp CD4 Bias
Immune Desert Mo Bias
Immune Desert Mp CD8 Bias
COL12A1
COL9A3
COL17A1
COL6A1
COL8A1
COL27A1
COL3A1
COL15A1
COL20A1
COL1A1
COL1A2
g
Spearman Correlation
M1
M2
COL1A1
COL1A2
COL3A1
COL4A1
COL4A2
COL5A1
COL5A2
COL6A2
COL6A3
COL6A1
COL12A1
COL18A1
h
[Collagen Transcriptional Signature]
High
Low
% Survival
Years

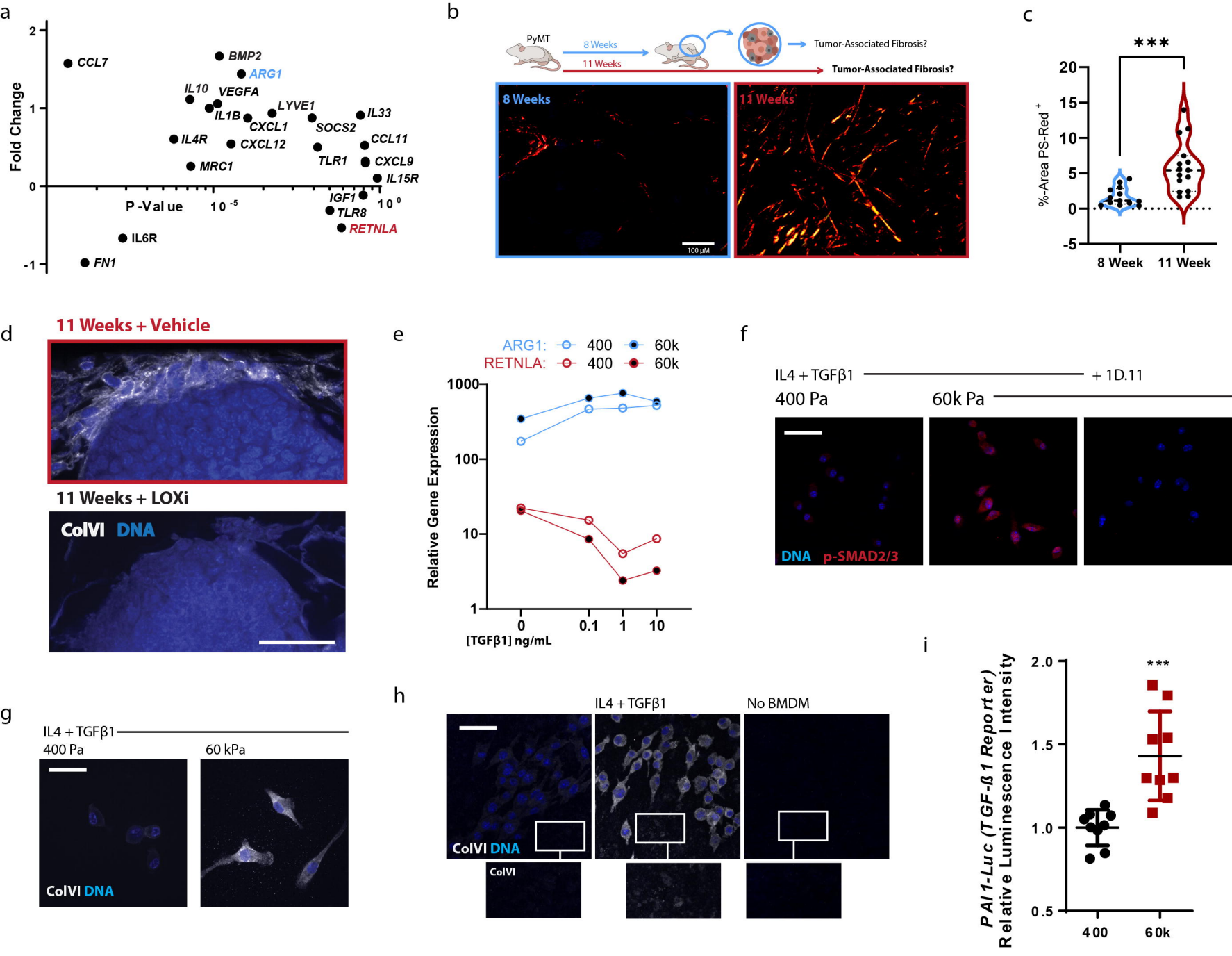
a
Fold Change
P-Value
CCL7
BMP2
ARG1
IL10
VEGFA
IL1B
LYVE1
CXCL1
SOCS2
IL33
IL4R
CXCL12
CCL11
MRC1
TLR1
CXCL9
IL15R
IGF1
TLR8
RETNLA
IL6R
FN1
b
PyMT
8 Weeks
11 Weeks
Tumor-Associated Fibrosis?
Tumor-Associated Fibrosis?
8 Weeks
11 Weeks
100 µM
c
***
%-Area PS-Red+
8 Week
11 Week
d
11 Weeks + Vehicle
11 Weeks + LOXi
ColVI DNA
e
ARG1: 400 60k
RETNLA: 400 60k
Relative Gene Expression
[TGFβ1] ng/mL
f
IL4 + TGFβ1
+ 1D.11
400 Pa
60k Pa
DNA p-SMAD2/3
g
IL4 + TGFβ1
400 Pa
60 kPa
ColVI DNA
h
IL4 + TGFβ1
No BMDM
ColVI DNA
ColVI
i
PAI1-Luc (TGF-ß1 Reporter)
Relative Luminescence Intensity
***
400
60k

5 transverse samples from 4 tumors per genotype
Distance in Pixels

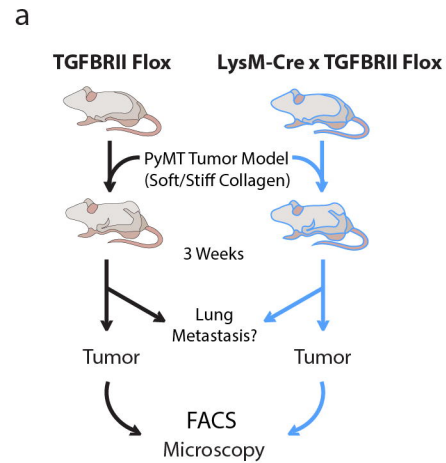

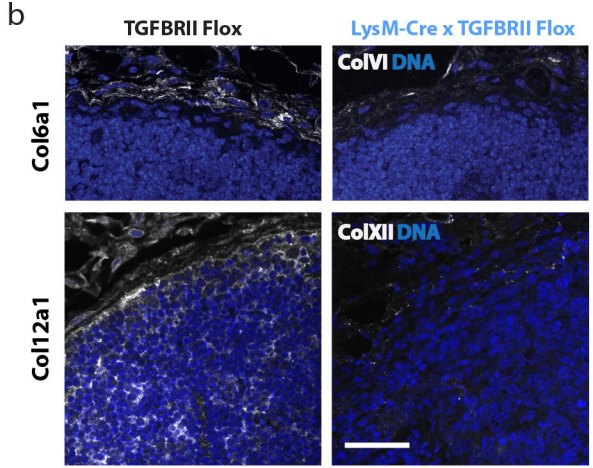

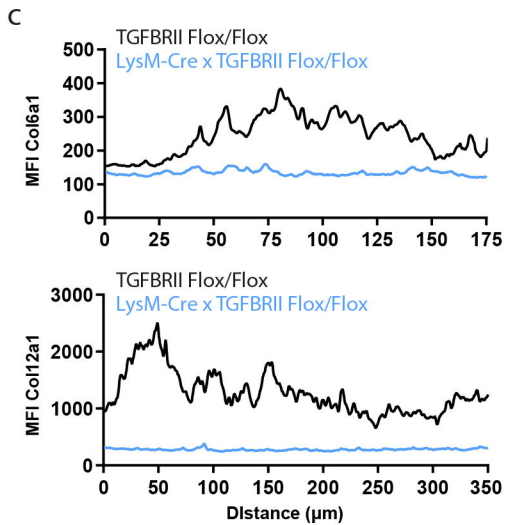

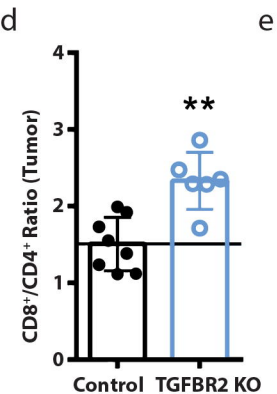

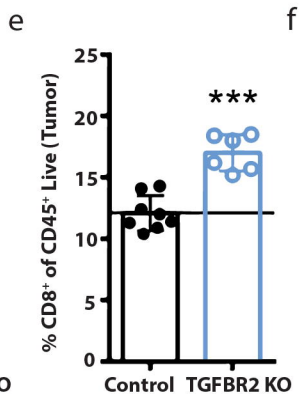

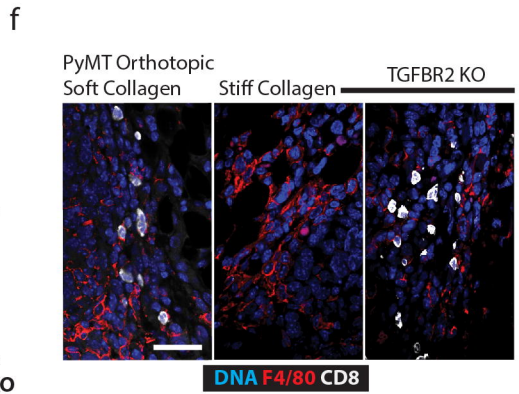

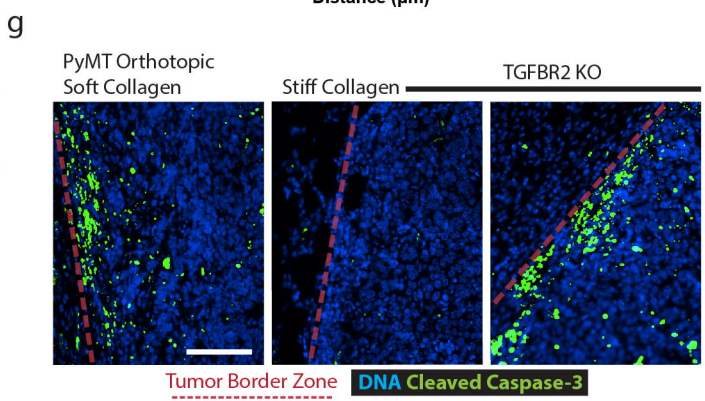

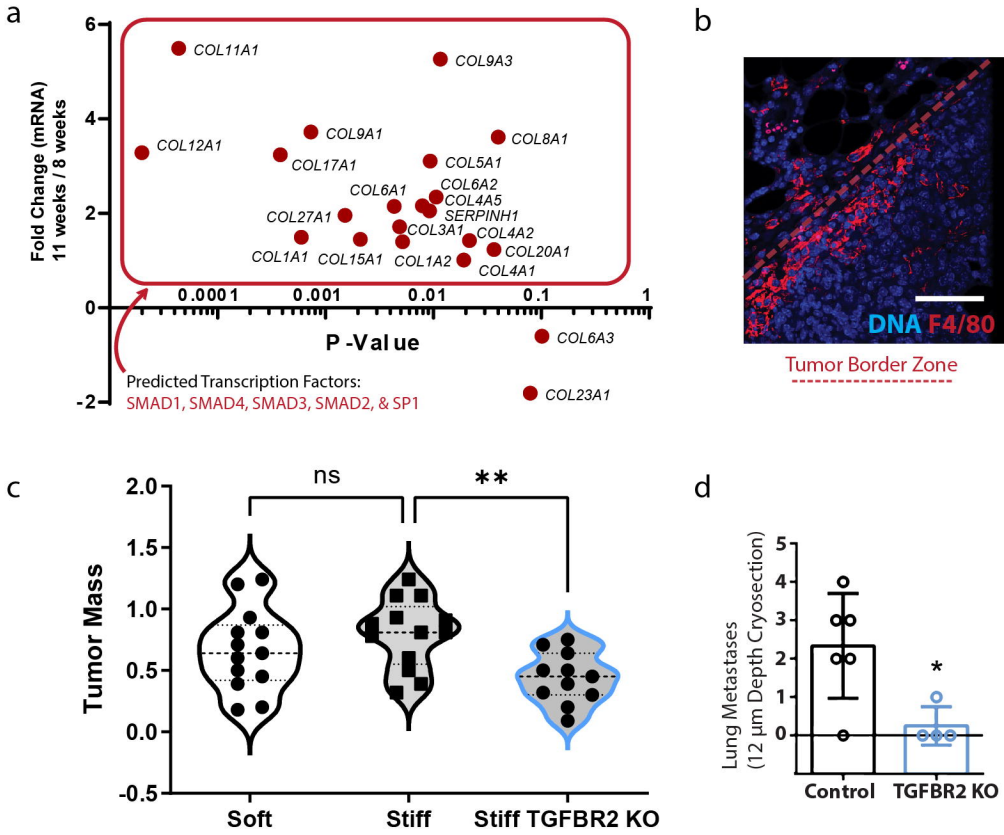
a
Fold Change (mRNA) 11 weeks / 8 weeks
P -Value
COL11A1
COL9A3
COL12A1
COL9A1
COL8A1
COL17A1
COL5A1
COL6A1
COL6A2
COL4A5
SERPINH1
COL27A1
COL3A1
COL4A2
COL1A1
COL15A1
COL1A2
COL20A1
COL4A1
COL6A3
COL23A1
Predicted Transcription Factors:
SMAD1, SMAD4, SMAD3, SMAD2, & SP1
b
DNA F4/80
Tumor Border Zone
c
Tumor Mass
ns
**
Soft
Stiff
Stiff TGFBR2 KO
d
Lung Metastases (12 µm Depth Cryosection)
*
Control
TGFBR2 KO

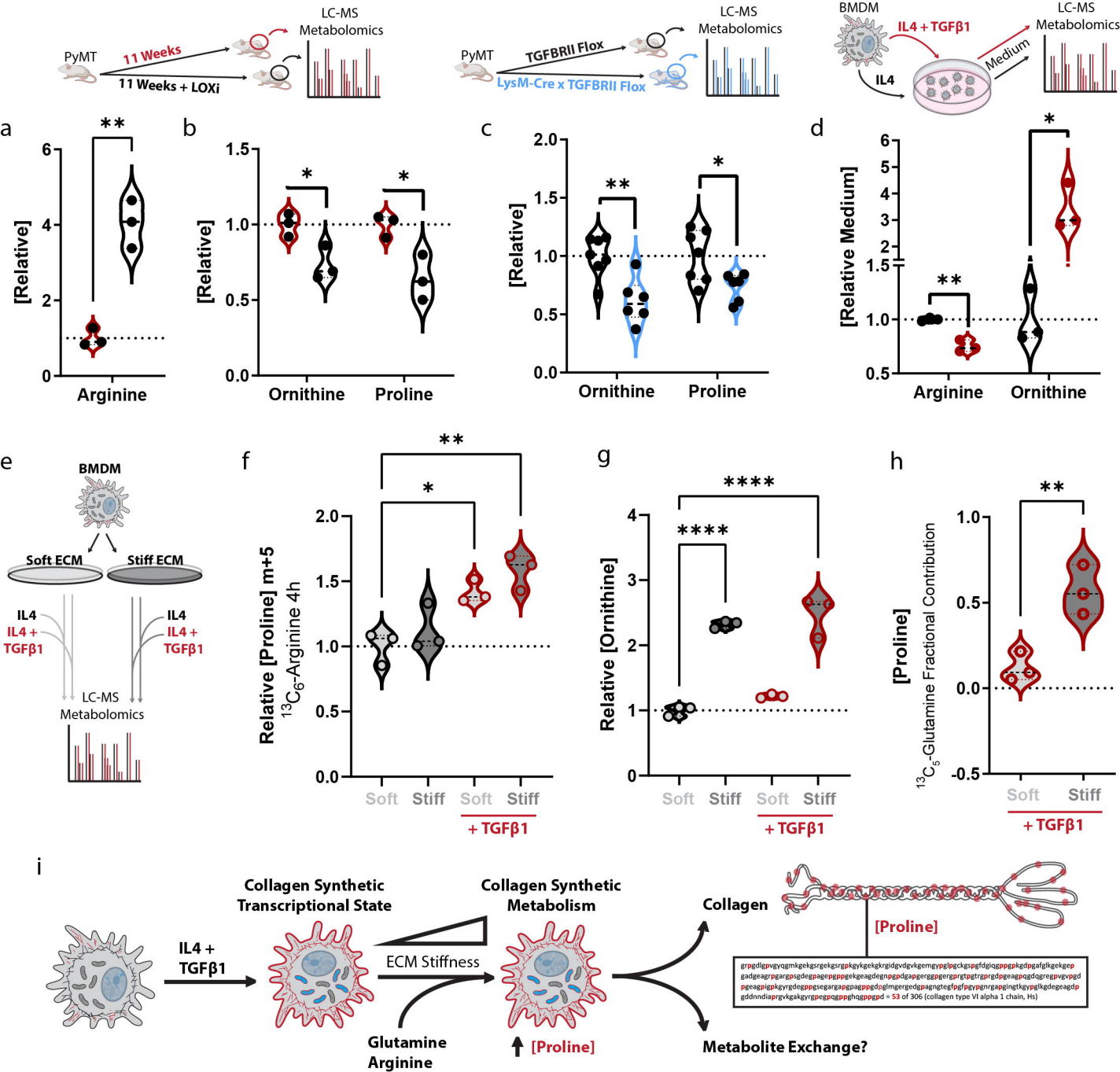
PyMT
11 Weeks
11 Weeks + LOXi
LC-MS Metabolomics
PyMT
TGFBRII Flox
LysM-Cre x TGFBRII Flox
LC-MS Metabolomics
BMDM
IL4 + TGFβ1
IL4
Medium
LC-MS Metabolomics
a
[Relative]
Arginine
b
[Relative]
Ornithine
Proline
c
[Relative]
Ornithine
Proline
d
[Relative Medium]
Arginine
Ornithine
e
BMDM
Soft ECM
Stiff ECM
IL4
IL4 + TGFβ1
IL4
IL4 + TGFβ1
LC-MS Metabolomics
f
Relative [Proline] m+5
13C6-Arginine 4h
Soft
Stiff
Soft
Stiff
+ TGFβ1
g
Relative [Ornithine]
Soft
Stiff
Soft
Stiff
+ TGFβ1
h
[Proline]
13C5-Glutamine Fractional Contribution
Soft
Stiff
+ TGFβ1
i
IL4 + TGFβ1
Collagen Synthetic Transcriptional State
ECM Stiffness
Collagen Synthetic Metabolism
Glutamine
Arginine
[Proline]
Collagen
[Proline]
Metabolite Exchange?

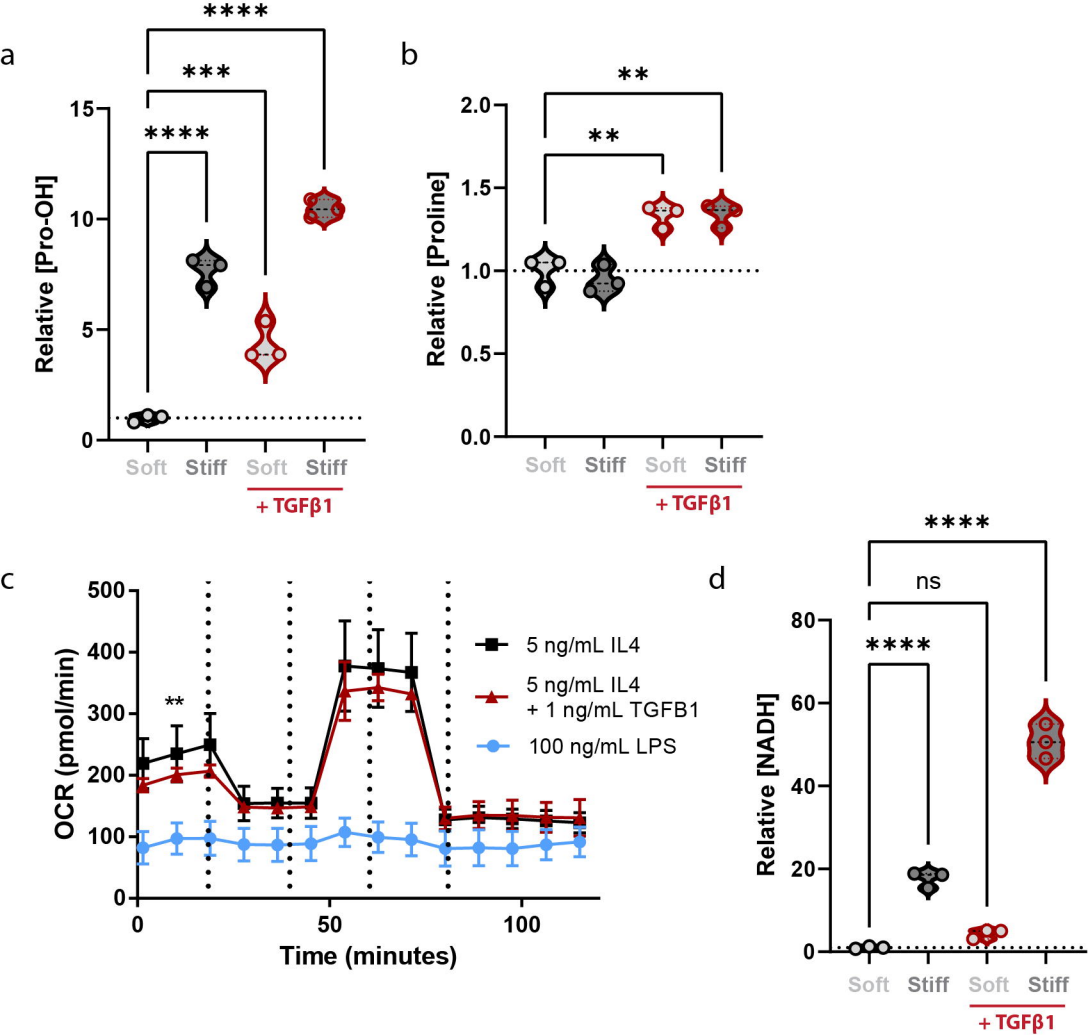
a
****
***
****
Relative [Pro-OH]
15
10
5
0
Soft
Stiff
Soft
Stiff
+ TGFβ1
b
**
**
Relative [Proline]
2.0
1.5
1.0
0.5
0.0
Soft
Stiff
Soft
Stiff
+ TGFβ1
c
OCR (pmol/min)
500
400
300
200
100
0
**
0
50
100
Time (minutes)
5 ng/mL IL4
5 ng/mL IL4
+ 1 ng/mL TGFB1
100 ng/mL LPS
d
****
ns
****
Relative [NADH]
80
60
40
20
0
Soft
Stiff
Soft
Stiff
+ TGFβ1

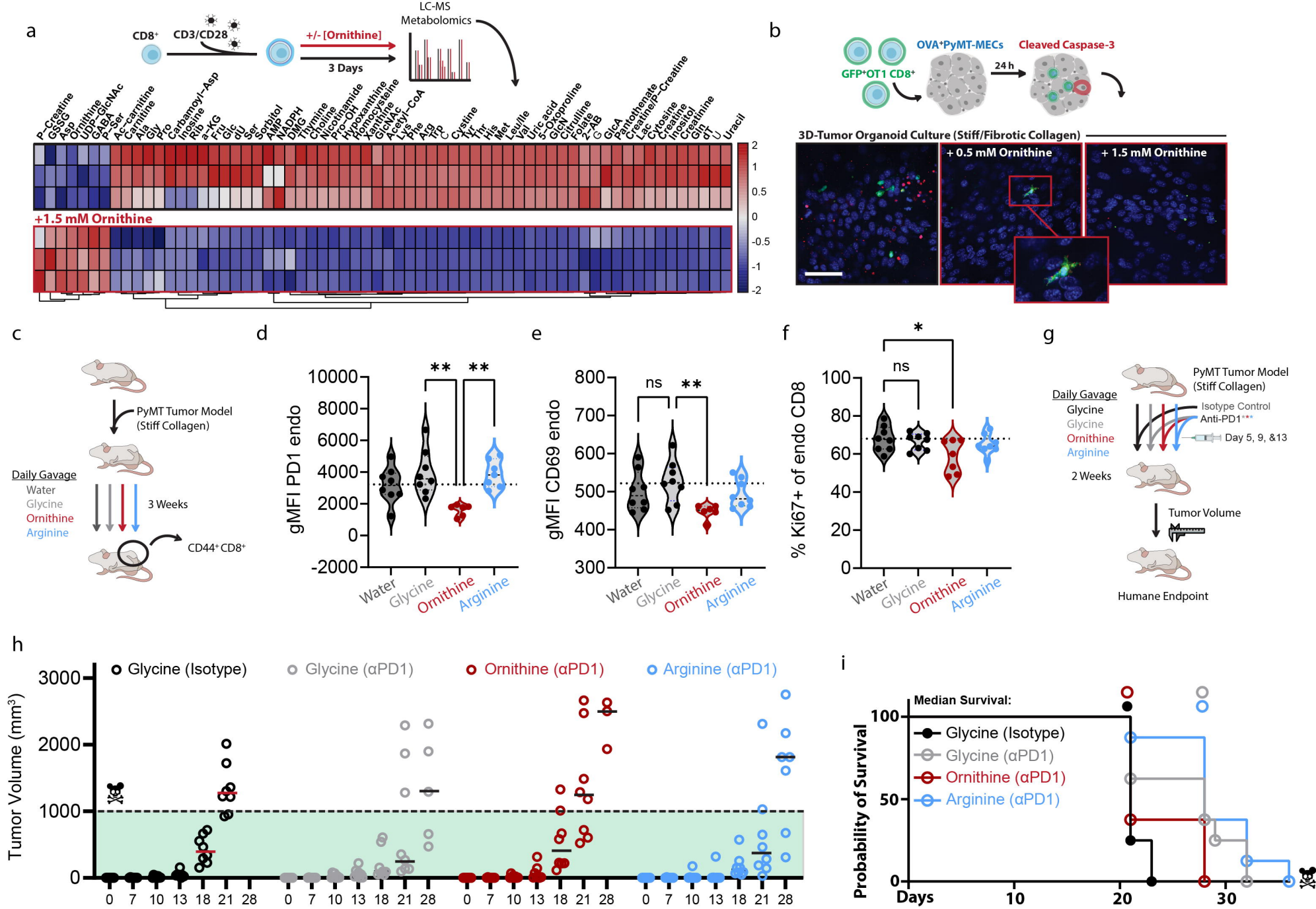
a
CD8+
CD3/CD28
+/- [Ornithine]
3 Days
LC-MS Metabolomics
+1.5 mM Ornithine
b
OVA+PyMT-MECs
Cleaved Caspase-3
GFP+OT1 CD8+
24 h
3D-Tumor Organoid Culture (Stiff/Fibrotic Collagen)
+ 0.5 mM Ornithine
+ 1.5 mM Ornithine
c
PyMT Tumor Model (Stiff Collagen)
Daily Gavage
Water
Glycine
Ornithine
Arginine
3 Weeks
CD44+ CD8+
d
gMFI PD1 endo
Water
Glycine
Ornithine
Arginine
e
gMFI CD69 endo
ns
f
% Ki67+ of endo CD8
g
PyMT Tumor Model (Stiff Collagen)
Isotype Control
Anti-PD1
Day 5, 9, &13
2 Weeks
Tumor Volume
Humane Endpoint
h
Tumor Volume (mm3)
Glycine (Isotype)
Glycine (αPD1)
Ornithine (αPD1)
Arginine (αPD1)
i
Median Survival:
Probability of Survival
Days

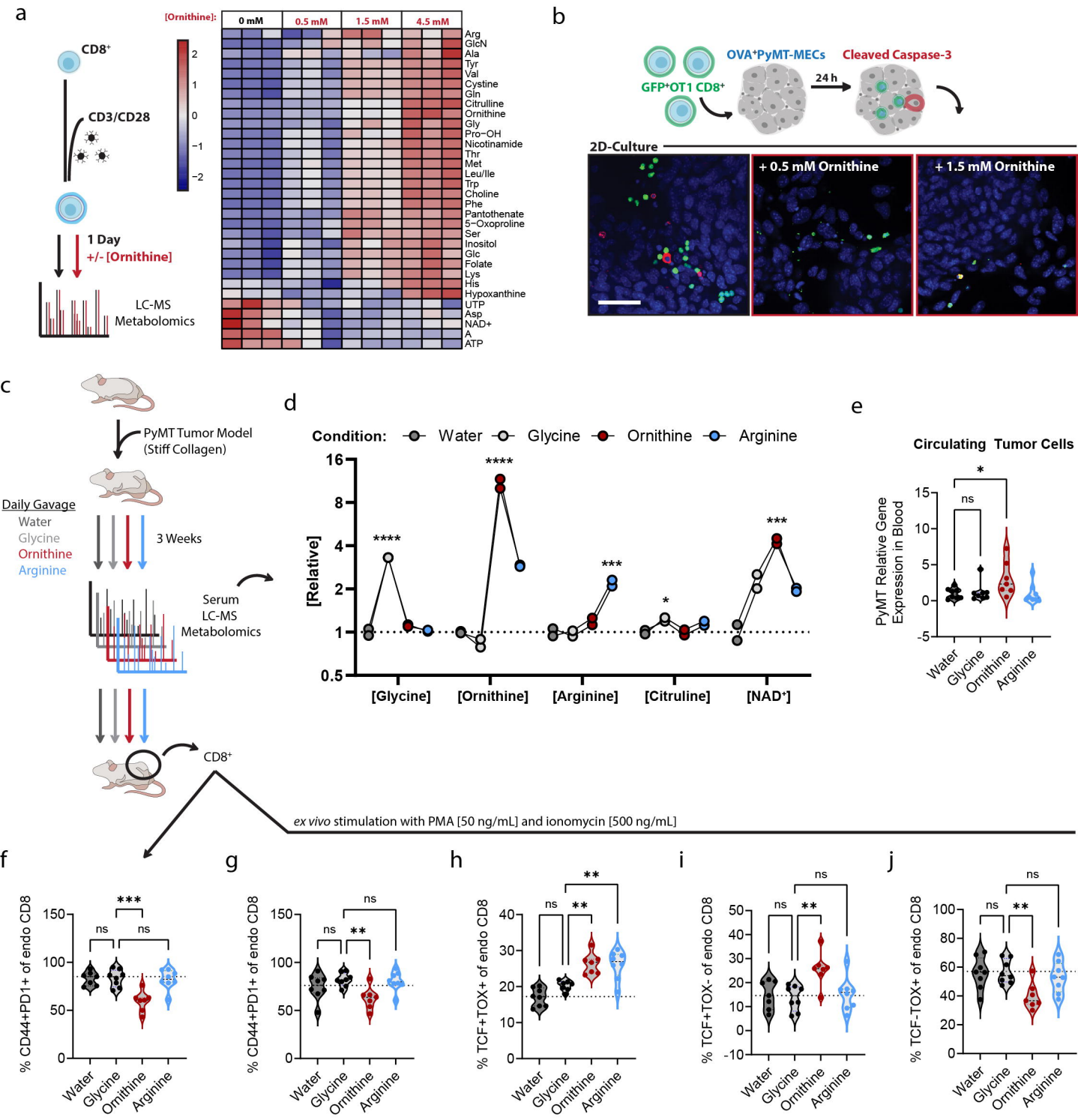
a
CD8+
CD3/CD28
1 Day
+/- [Ornithine]
LC-MS
Metabolomics
[Ornithine]:
0 mM
0.5 mM
1.5 mM
4.5 mM
Arg
GlcN
Ala
Tyr
Val
Cystine
Gln
Citrulline
Ornithine
Gly
Pro−OH
Nicotinamide
Thr
Met
Leu/Ile
Trp
Choline
Phe
Pantothenate
5−Oxoproline
Ser
Inositol
Glc
Folate
Lys
His
Hypoxanthine
UTP
Asp
NAD+
A
ATP
b
OVA+PyMT-MECs
Cleaved Caspase-3
GFP+OT1 CD8+
24 h
2D-Culture
+ 0.5 mM Ornithine
+ 1.5 mM Ornithine
c
PyMT Tumor Model
(Stiff Collagen)
Daily Gavage
Water
Glycine
Ornithine
Arginine
3 Weeks
Serum
LC-MS
Metabolomics
CD8+
ex vivo stimulation with PMA [50 ng/mL] and ionomycin [500 ng/mL]
d
Condition:
Water
Glycine
Ornithine
Arginine
[Relative]
[Glycine]
[Ornithine]
[Arginine]
[Citruline]
[NAD+]
e
Circulating Tumor Cells
PyMT Relative Gene Expression in Blood
ns
f
% CD44+PD1+ of endo CD8
g
% CD44+PD1+ of endo CD8
h
% TCF+TOX+ of endo CD8
i
% TCF+TOX- of endo CD8
j
% TCF-TOX+ of endo CD8

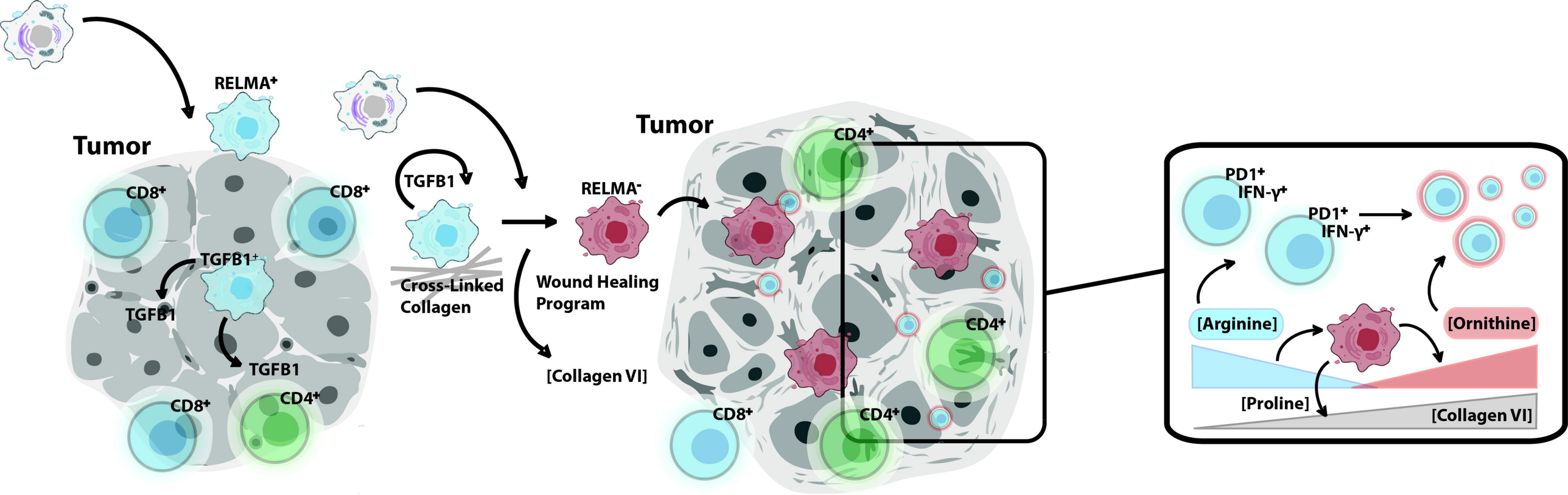
RELMA+
Tumor
CD8+
CD8+
TGFB1+
TGFB1
TGFB1
CD8+
CD4+
TGFB1
Cross-Linked
Collagen
RELMA-
Wound Healing
Program
[Collagen VI]
Tumor
CD4+
CD4+
CD8+
CD4+
PD1+
IFN-γ+
PD1+
IFN-γ+
[Arginine]
[Ornithine]
[Proline]
[Collagen VI]